TECHNISCHE
UNIVERSITÄT
WIEN
Vienna University of Technology

DIPLOMARBEIT

Monte-Carlo Raytracing for Thermal Transport Simulation

ausgeführt am Institut für

Mikroelektronik
der Technischen Universität Wien

unter der Anleitung von
Prof. Hans Kosina

durch

Stefanie Wolf
Baumeisterg. 6/47/3
1160 Wien

Datum

Unterschrift

Contents

Abstract

Heat transport in crystalline semiconductors occurs by quantized lattice vibrations called phonons. The Boltzmann Transport Equation (BTE) models both equilibrium and non-equilibrium heat conduction when wave effects are negligible. Non-equilibrium heat conduction occurs either at low temperatures or small length scales. The BTE does not treat the individual positions and momenta of each particle in the medium, but rather deals with the probability density function of an ensemble of particles. Free flight and scattering are represented as operators in the BTE. The Monte-Carlo (MC) method is widely used for the solution of the BTE.

A computationally efficient MC algorithm for heat transport in semiconductors has been developed in this work. The method accounts for longitudinal and transversal polarizations of acoustic phonon propagation and non-linear dispersion relations. Deterministic boundary scattering and stochastic normal and Umklapp phonon scattering are treated. The algorithm yields temperature and energy distributions, and the thermal conductivity of the simulated structure. The following studies are carried out:

The time-of-flight (TOF) of phonons in thin Si-films and nanowires is calculated in dependence of geometric properties of the device such as lengths, aspect ratios and surface roughness while neglecting phonon-phonon scattering. An increase of the TOF with partially diffusive boundary scattering is observed, indicating that diffusive surface scattering plays a much more important role for dimensions below 100 nm.

The thermal conductivity of bulk Si including phonon-phonon scattering is calculated and benchmarked against measurement results. At low temperatures size effects are observed because the phonon mean free path (MFP) becomes larger than the length of the device. Using a temperature-dependent MFP scaling factor good agreement with measurement data is achieved in a temperature range between 15 K and 400 K.

Nanomeshes in form of nanoporous Si membranes are investigated. The thermal conductivity at room temperature is calculated for two arrangements of the holes: rectangular and hexagonal. For structures with 50% porosity the thermal conductivity is found to be significantly lower than in bulk (as low as 9 W/mK) which is in good agreement with recent experimental data.

Kurzfassung

In kristallinen Halbleitern erfolgt der Wärmetransport durch quantisierte Gitterschwingungen, genannt Phononen. Die Boltzmann-Transport-Gleichung (BTE) beschreibt die Wärmeleitung sowohl im thermodynamischen Gleichgewicht, als auch im Nicht-Gleichgewicht, wenn die Welleneigenschaften der Phononen vernachlässigbar sind. Wärmeleitung im Nicht-Gleichgewicht erfolgt bei niedrigen Temperaturen und in Strukturen mit kleinen Längenskalen. Anstatt der Positionen und Impulse der Teilchen, wird in der BTE die Wahrscheinlichkeitsdichtefunktion von einem Ensemble beschrieben. Freier Flug und Streuung werden in der BTE durch Operatoren repräsentiert. Monte-Carlo (MC) ist eine häufig verwendete Methode zur Lösung der BTE.

In dieser Arbeit wurde ein MC-Simulator zur Berechnung des Wärmetransports in Halbleitern entwickelt. Die Methode beschreibt akustische Phononen longitudinaler und transversaler Polarisation und deren nichtlineare Dispersionsrelationen. Deterministische Streuung an den Grenzflächen und stochastische Phonon-Phonon-Streuung sind implementiert. In den Simulationen werden Temperatur-, Energieverteilung und die thermische Leitfähigkeit der untersuchten Strukturen berechnet. Die folgenden Studien wurden durchgeführt.

In Abhängigkeit von geometrischen Eigenschaften der Struktur, wie Längen, Seitenverhältnissen und Oberflächenrauhigkeit wird die Flugzeit (TOF) in dünnen Si-Filmen und Nanowires unter Vernachlässigung von Phononen-Streuung berechnet. Die TOF steigt mit diffuser Streuung an den Grenzflächen, die eine wichtige Rolle bei Längen kleiner als 100 nm spielt.

Die thermische Leitfähigkeit eines Si-Einkristalls wird unter Berücksichtigung von Phononen-Streuung simuliert. Bei niedrigen Temperaturen werden Größeneffekte beobachtet, da die mittlere freie Weglänge (MFP) der Phononen größer als die Länge der simulierten Struktur ist. Mit einem temperaturabhängigen MFP-Skalierungsfaktor wird gute Übereinstimmung zu Messdaten im Bereich von 15 K bis 400 K erzielt.

Nanomeshes in Form nanoporöser Si-Membrane werden untersucht. Die thermische Leitfähigkeit bei Raumtemperatur wird für rechteckige und hexagonale Anordnungen der Löcher berechnet. Übereinstimmend mit experimentellen Daten sinkt in Strukturen mit 50 % Porosität die thermische Leitfähigkeit ($\approx 9\,\mathrm{W/mK}$) deutlich gegenüber dem Einkristall.

Acknowledgements

First, I would like to acknowledge my advisor Professor Hans Kosina, for giving me the opportunity to do this thesis. I am also grateful to Zlatan Stanojevic and Neophytos Neophytou for their guidance, patience, and help. I would also like to thank Hossein Karamitaheri for useful discussions, Klaus Schnass for support with the GTS-Framework, and Oskar Baumgartner for providing me with his random number generator.

And finally I am grateful to have the support of my family and Matthias.

Chapter 1

Introduction

Thermoelectric devices are solid state devices capable of converting heat directly into electrical energy, making them ideal candidates for renewable energy conversion. Thermoelectric devices are also used for refrigeration and temperature measurement purposes.

Global energy consumption is expected to rise in the future. This and environmental concerns about the use of fossil fuels require the reduction of the fossil fuels' share of the energy supply and the expansion of renewable energy sources. Thermoelectric energy falls into that category. Waste heat is generated in many fields, i.e. in industrial processes and in the exhausts of cars. Using thermoelectric devices part of the waste heat can be turned to electricity. The efficiency of thermoelectric converters is determined by the figure of merit $ZT = S^2\frac{\sigma}{\kappa}T$, where S is the Seebeck coefficient, σ is the electrical conductivity and κ is the thermal conductivity. The practicality of thermoelectric generators is limited by the low figure of merit, $ZT \sim 1$. The most commonly used thermoelectric material is bismuth telluride ($\mathrm{Bi_2Te_3}$), which has the disadvantages of high manufacturing costs, low availability and toxicity. Nano-structured thermoelectric devices have recently gained much attention as they demonstrate the availability of achieving conversion efficiencies much higher than those observed in bulk materials [10].

Nano-structured materials are of high interest due to their potential of suppressing the thermal conductivity, which increases ZT. Si in comparison to $\mathrm{Bi_2Te_3}$ is abundant. Due to its high lattice thermal conductivity ($\kappa = 142\,\mathrm{W/(mK)}$) bulk Si has not been considered for thermoelectric applications to date. In Si nanowires, however, an almost 100-fold suppression in thermal conductivity was recently achieved resulting in an enhancement of ZT from

0.01 for bulk to $0.4 - 0.6$ [15, 16]. However, the strong performance variation with diameter and surface roughness and stability issues make large scale implementations of nanowires a challenge.

In another approach, thin nanoporous membranes made of single-crystalline Si are investigated [14]. These have the advantages of easy manufacturing and good mechanical strength. Si nanomeshes exhibit reproducibly low thermal conductivity, while maintaining sufficient electrical conductivity. The ZT value of nanomeshed Si with a hexagonal pattern of holes and 35% porosity was measured to be 0.4 at room temperature [14].

The modelling of nano-structured thermoelectric devices requires the treatment of non-equilibrium heat transport. In this non-equilibrium regime it is necessary to solve the Boltzmann transport equation (BTE) for phonons. In this work the Monte-Carlo method is used. The Monte-Carlo method is a standard tool for solving the BTE for electrons [6], phonons [4, 5], and other particles. Due to their lack of charge, phonons are unaffected by fields, and therefore travel in straight lines until they either scatter (stochastic process) or reach a device boundary (deterministic process). The computation of the phonon trajectories is done using a raytracing algorithm combined with a random process for the scattering events.

In this thesis the developed simulation method is described and results are benchmarked against the thermal conductivity of bulk Si over a large range of temperatures. Finally, the method is applied to compute the thermal conductivity of nanomeshes.

Chapter 2

Theory

2.1 Crystal vibrations - phonons

A crystal is a three-dimensional periodic array of identical building blocks (primitive cells), forming a translationally invariant lattice. In a simple model, the crystal lattice can be visualized as an array of point-masses representing individual atoms or molecules and springs representing bonding forces. The forces between each pair of atoms may be characterized by a potential energy function $V(r)$ that depends on the distance of separation of the atoms. The bonding forces are necessary to keep the masses at their equilibrium position. Due to the bonding forces between atoms, the displacement of one or more atoms from their equilibrium positions will give rise to a set of vibration waves propagating through the lattice. The energy of a lattice vibration is quantized and each quantum is called a phonon. A phonon is a travelling wave with angular frequency ω, wave vector $\mathbf{k}$ and group velocity $\mathbf{v}_{\mathrm{g}}$. The energy of a phonon is given by $\hbar\omega$, where $\hbar$ is the reduced Planck's constant.

In a crystal with (at least) two atoms per primitive cell, the dispersion relation $\omega(k)$ exhibits two branches, known as the optical and the acoustic branches. As shown in Fig. 2.1, for optical modes the two atoms in the unit cell have opposite phases, while for acoustic modes they are in phase. For acoustic phonons the dispersion relation is almost linear at low values of k, whereas for optical phonons $\omega(0) \neq 0$. In three dimensions, oscillations are not restricted to the direction of propagation (longitudinal), but also occur in the perpendicular plane (transversal). Due to the periodicity of a crystal the range of physically relevant values for the wave vector $\mathbf{k}$ is given by the first Brillouin zone, which is the primitive unit cell in the reciprocal lattice. The first Brillouin zone is specified by $-\frac{\pi}{a} \leq k \leq \frac{\pi}{a}$, where a is the lattice parameter. In Fig. 2.2 we plot a quadratic fit of the dispersion relation of Si along the [100] direction, the one employed in our model as Ref.[5]. The full dispersion relation is shown in Fig. 2.3. Here, the dispersion has been calculated using the modified valence force field (MVFF) method [18] and the results are in excellent agreement with experimental data [19]. Because of their slow group velocity, optical phonons do not contribute significantly to thermal transport [4]. Therefore, their influence is neglected onwards. We account for the longitudinal acoustic (LA) and the two-fold degenerate transversal acoustic (TA) branch in Si, which is the material of interest in this work.

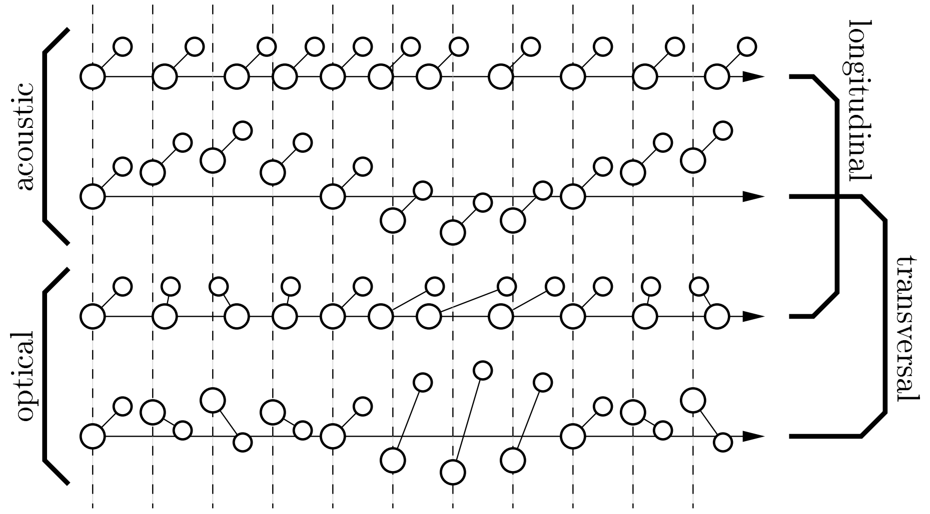

Figure 2.1: Particle displacement of transverse optical and acoustical phonons at the same wavelength [8].

In thermal equilibrium, the temperature T of a medium is well defined and the probability of finding a phonon with angular frequency $\omega = 2\pi\nu$ is given by the Bose-Einstein distribution [1]:

$$\langle n \rangle = \frac{1}{\exp(\frac{\hbar\omega}{k_\mathrm{B}T}) - 1}, \tag{2.1}$$

where k_B is the Boltzmann constant and $\langle n \rangle$ is the occupation number.

Assuming the restoring force is proportional to the displacement, the energy of a phonon is given by the eigenvalues of the harmonic oscillators for

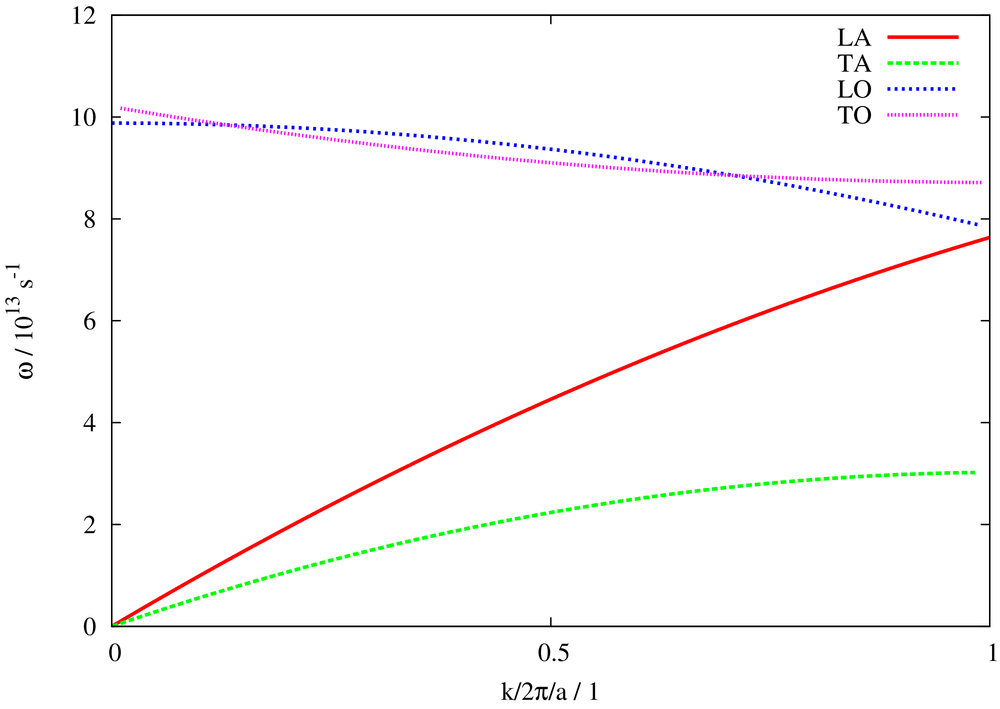

Figure 2.2: Quadratic fit [2] for the dispersion relation of longitudinal acoustic (LA), transversal acoustic (TA), longitudinal optical (LO) and transversal optical (TO) phonons along the [100] direction in Si for $0 \leq k \leq \frac{2\pi}{a}$.

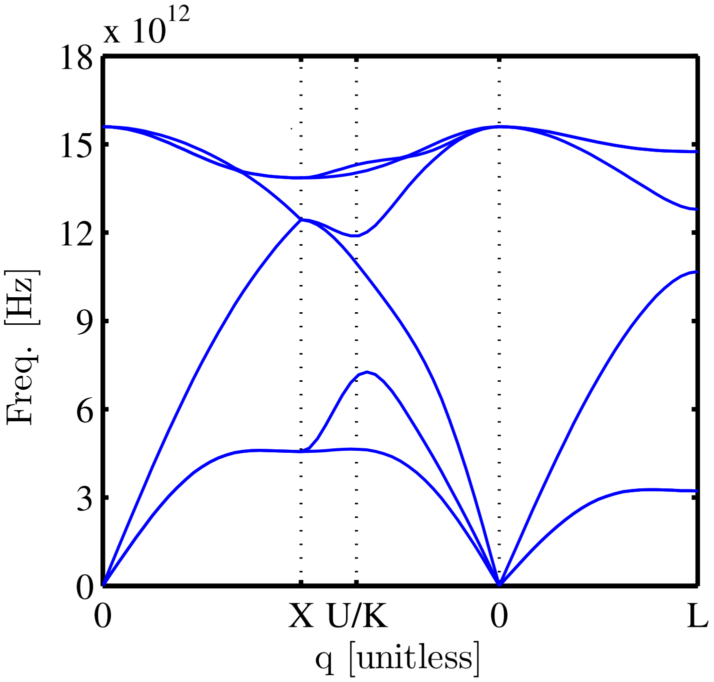

Figure 2.3: Dispersion relation calculated in Ref. [18] using the modified valence force field (MVFF) method. 0 denotes the Γ point which is the Brillouin zone center. Starting from 0 towards X shows the [100] direction. Starting from the next 0 towards U/K and then to X is the dispersion relation for the [110] direction. And finally from the right-hand 0 to L indicates the [111] direction.

the mode ω,

$$E_n = \left(n + \frac{1}{2}\right)\hbar\omega. \tag{2.2}$$

Therefore, the total thermal energy is given by

$$E = \sum_p \sum_{\mathbf{k}} \left(\langle n\rangle + \frac{1}{2}\right)\hbar\omega. \tag{2.3}$$

In Eq. 2.3 the sum is performed over all relevant phonon polarizations p (longitudinal acoustic and transverse acoustic), and wave vectors, $\mathbf{k}$. The wave vector space over which the summation is performed is the first Brillouin zone (BZ).

Assuming that for large crystals the wave vector space is very dense, the summation can be replaced by an integration,

$$E = \frac{V}{(2\pi)^3} \sum_p \int_{\mathrm{BZ}} \left(\langle n \rangle + \frac{1}{2} \right) \hbar\omega \mathrm{d}\mathbf{k}. \tag{2.4}$$

Supposing that the number of vibrational states in the frequency range ω to $\omega + d\omega$ is given by the density of states $D(\omega)d\omega$, then the energy can be calculated as:

$$E = V \sum_p \int_0^\infty \left(\langle n \rangle + \frac{1}{2} \right) \hbar\omega D(\omega) \mathrm{d}\omega. \tag{2.5}$$

Assuming isotropy, the density of states $D(\omega)$ is expressed as:

$$D(\omega) = \frac{k^2}{2\pi^2} \frac{\mathrm{d}k}{\mathrm{d}\omega}, \tag{2.6}$$

where $k = k(\omega, p)$ is the dispersion relation.

The group velocity v_g of a phonon is given by the slope of the dispersion relation,

$$v_\mathrm{g} = \frac{\mathrm{d}\omega}{\mathrm{d}k}. \tag{2.7}$$

In Fig. 2.4 we plot the group velocity v_g of the acoustic branches in Si.

The constant 1/2 term of Eq. 2.2 is called zero-point energy, does not contribute to energy transfer and is therefore neglected. Using the definition of the group velocity and accounting for the degeneracy of the dispersion branches g_p, the total vibrational energy is calculated as [4]:

$$E = V \sum_p \int_0^\infty \left(\frac{\hbar\omega}{\exp(\frac{\hbar\omega}{k_\mathrm{B}T}) - 1} \right) g_\mathrm{p} \frac{k^2}{2\pi^2 v_\mathrm{g}} \mathrm{d}\omega \tag{2.8}$$

Phonon scattering As phonons travel through the material they can scatter through several mechanisms. These mechanisms include scattering due to anharmonic terms of the potential, scattering due to lattice imperfections, phonon-electron and boundary scattering. Anharmonic interactions of the third order involve three-phonons, e.g. two phonons are annihilated to create one phonon or vice versa. There are two kinds of anharmonic-phonon processes: normal processes (N) which preserve momentum, and Umklapp

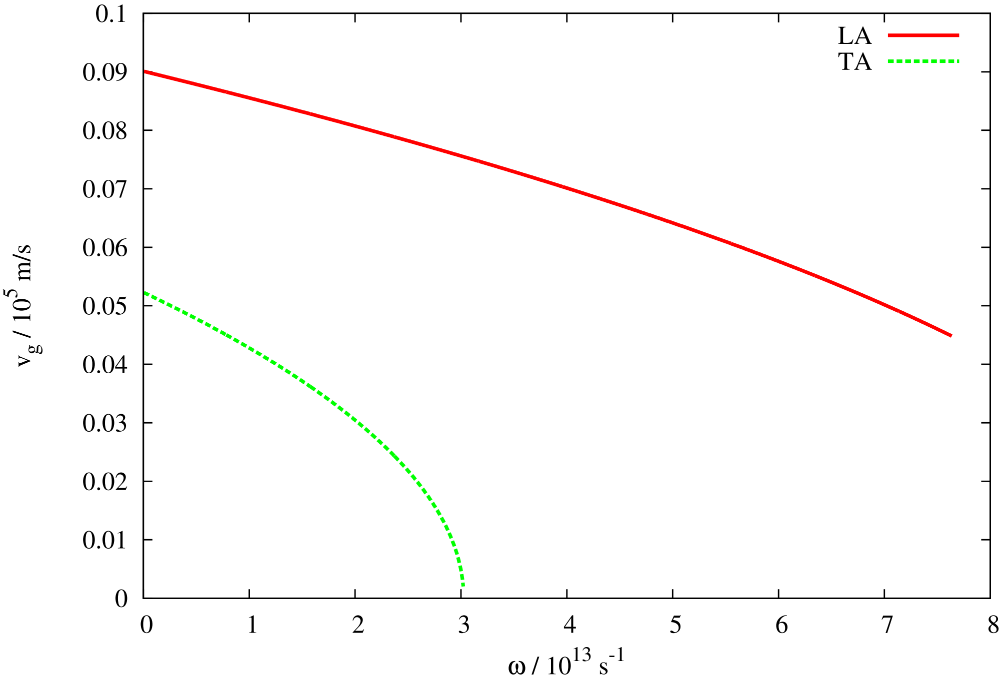

Figure 2.4: Group velocity of longitudinal acoustic (LA) and transversal acoustic (TA) phonons along the (100) direction in Si.

processes (U) which satisfy momentum conservation by means of a reciprocal lattice vector $\mathbf{G}$ as:

$$\begin{aligned} \mathbf{k}_1 + \mathbf{k}_2 \Leftrightarrow & \quad \mathbf{k}_3 \quad \text{normal} && (2.9) \\ \mathbf{k}_1 + \mathbf{k}_2 \Leftrightarrow & \quad \mathbf{k}_3 + \mathbf{G} \quad \text{Umklapp.} && (2.10) \end{aligned}$$

For both normal and Umklapp processes the energy is conserved,

$$\begin{aligned} \omega_1 + \omega_2 = & \quad \omega_3 \quad \text{annihilate phonon} && (2.11) \\ \omega_1 = & \quad \omega_2 + \omega_3 \quad \text{create phonon.} && (2.12) \end{aligned}$$

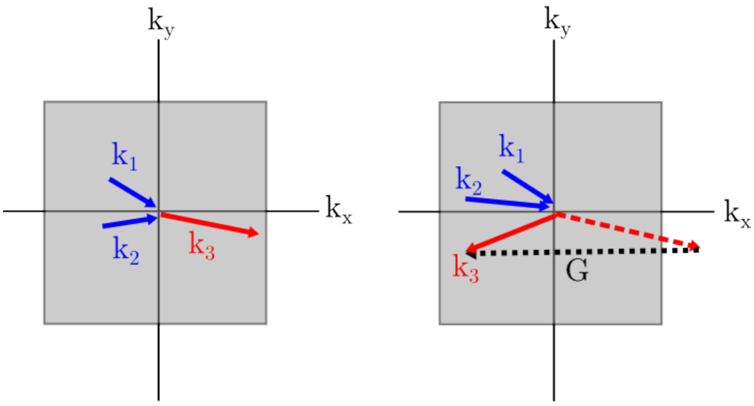

normal scattering **umklapp scattering**

Figure 2.5: (a) Normal and (b) Umklapp phonon collisions in a two-dimensional square lattice. The grey square represents the first Brillouin zone in k-space. $G = 2\pi/a$ where a is the lattice constant of the crystal. In the Umklapp process the direction of the x-component of the phonon flux is reversed.

As shown in Fig. 2.5, the Umklapp process directly poses resistance to energy transport, as the direction of the heat flux is reversed. The normal process only indirectly affects the transport process by modifying the frequency distribution of phonons, but not thermal conductivity directly. At high temperatures $T > \theta_{\text{Debye}}$ all phonon modes are excited, because $k_{\text{B}}T > \hbar\omega_{\text{max}}$ and Umklapp scattering becomes the dominant process.

Each scattering mechanism can be characterized by relaxation time τ or a relaxation rate $1/\tau$. All scattering processes contribute to a combined relaxation time τ_C using Matthiessen's rule

$$\frac{1}{\tau_{\text{C}}} = \frac{1}{\tau_{\text{U}}} + \frac{1}{\tau_{\text{N}}} + \left(\frac{1}{\tau_{\text{imp}}} + \frac{1}{\tau_{\text{ph-e}}} + \frac{1}{\tau_{\text{B}}} \right). \qquad (2.13)$$

In this work phonon-phonon and phonon-boundary-scattering processes are included.

2.2 Thermoelectricity

Thermoelectric phenomena are known more specifically as the Seebeck effect (converting a temperature difference to current), Peltier effect (converting current to a temperature difference) and Thomson effect (describing the heating or cooling of a current-carrying conductor with a temperature gradient). While all conducting materials have a nonzero thermoelectric effect, in most the effect is too small. Commonly used thermoelectric materials are bismuth telluride (Bi_2Te_3) or lead telluride (PbTe). The application of these materials is limited due to the material's limited availability, toxicity and high cost.

2.2.1 Seebeck effect

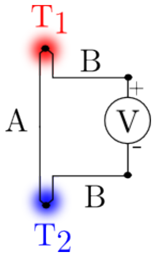

Figure 2.6: Circuit for measuring the Seebeck effect. A and B are two dissimilar conductors. For example, A and B can be two different metals or semiconductors with unequal doping. The junctions are kept at different temperatures T_1 and T_2.

We consider a circuit formed from two dissimilar conductors A and B which are connected electrically via two junctions. If the junctions are kept at different temperatures T_1 and T_2 a voltage

$$V = \int_{T_1}^{T_2} \left(S_{\mathrm{B}}(T) - S_{\mathrm{A}}(T)\right) \mathrm{d}T. \tag{2.14}$$

can be measured, where S_{A} and S_{B} are material-dependent Seebeck coefficients. Typical values for the Seebeck coefficients in metals are

$10^{-5}\,\mathrm{V/K} to 10^{-6}\,\mathrm{V/K}$ and in semiconductors $10^{-3}\,\mathrm{V/K}$ [11]. The Seebeck coefficient is a function of temperature and doping.

The Seebeck effect's underlying physical phenomenon is charge-carrier diffusion. Due to the temperature difference, the number of excited charge-carriers is larger at the high-temperature end. Therefore, hot carriers diffuse from the hot end to the cold end and vice versa. If the device were left to reach thermodynamic equilibrium, this would result in heat being distributed evenly throughout the device. A constant diffusion flux is reached, when the temperature difference at the device ends is kept constant. If the rate of diffusion of hot and cold carriers in opposite directions is equal, there is no net change in charge. Scattering with phonons or impurities limits the diffusion flux. If the hot and cold carriers diffuse at different rates, they build up charge at one end of the material, and thus a difference in the electrostatic potential.

2.2.2 Thermoelectric figure of merit

Thermoelectric efficiency is quantified by the dimensionless figure of merit ZT given by:

$$ZT = S^2 \frac{\sigma}{\kappa} T \tag{2.15}$$

where S is the Seebeck coefficient or thermopower, σ is the electrical conductivity, κ is the thermal conductivity and T is the temperature [10]. The term $S^2\sigma$ is referred to as the power factor.

Typically materials with $ZT \gtrsim 1$ are considered as promising for thermoelectric applications. Bi_2Te_3 has the figure of merit 1 at room temperature. Because S, σ and κ are adversely interrelated, there is no straight forward way to optimize ZT.

2.2.3 Engineering of the thermal conductivity

To optimize the figure of merit, there are several design principles. One of them is the concept of a “phonon-glass-electron-crystal” [10], a material that conducts heat poorly as in a glass, but conducts charge as a in crystal. The total thermal conductivity is given by

$$\kappa = \kappa_\mathrm{e} + \kappa_\mathrm{l} \tag{2.16}$$

where κ_e and κ_l are the electronic and lattice contributions to κ. In Si and most common semiconductors $\kappa_\mathrm{l} \ll \kappa_\mathrm{e}$. Therefore, it is only necessary to minimize κ_l, which can be achieved in different ways:

Reduced dimensions: If in the bulk material the mean free path λ_p of phonons is larger than that of charge carriers λ_e, then it is useful to introduce a reduced dimension l with $\lambda_\mathrm{p} < l < \lambda_\mathrm{e}$. Thus phonons experience severe boundary scattering, while charge transport remains almost unaltered. This approach has been successfully demonstrated with Si nanowires.

Nano-crystalline approaches: Nano-crystalline approaches work in a similar fashion. If the material's grain size is smaller than the mean free path of phonons λ_p, then phonons are strongly scattered on the grain boundaries.

Superlattices: Significant enhancements of ZT were reported in Bi_2Te_3/Bi_2Se_3 superlattices and PbTe/PbTeSe quantum dot superlattices. The superlattice leads to partially diffuse interface scattering and modification of the phonon modes and thus a potentially reduced group velocity. The fabrication of superlattices involves thin film growth methods and is therefore too expensive for large scale applications.

Phonon reflectivity: By using layers of mismatched materials, the thermal conductivity perpendicular to interfaces can be reduced. Phonons experience diffuse interface scattering which increases phonon reflectivity. Mismatch between bulk dispersion relations of the adjacent materials localizes phonons.

2.2.4 Thermoelectric devices

Semiconducting thermoelectric devices usually consist of pairs of p- and n-type elements as shown in Fig. 2.7. When a heat source is provided, the thermoelectric device functions as a power generator based on the Seebeck effect. The heat source drives electrons in the n-type element toward the cooler region, creating a current through the circuit. Holes in the p-type element then flow in the direction of the current. The same devices can act as coolers through the Peltier effect.

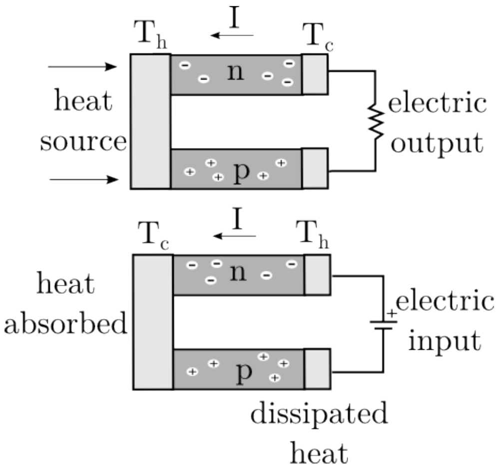

Figure 2.7: Schematic setup of thermoelectric generators (top) and refrigerators (bottom).

2.3 Boltzmann transport equation

The Boltzmann transport equation (BTE) is used to describe the transport of phonons in a crystal lattice when wave effects are negligible. Generally, the BTE is used to model the statistical distribution of particles, which are either in thermal equilibrium or non-equilibrium. In case of phonons, non-equilibrium heat conduction occurs either when the length scales of the device are small or at low temperatures. The equation does not treat the individual positions and momenta of each particle in the medium, but rather considers the probability density function $f(t, \mathbf{r}, \mathbf{k})$ of an ensemble of particles. The distribution function is a function of the independent variables time t, position $\mathbf{r}$, and momentum $\mathbf{k}$. Using the distribution function $f(t, \mathbf{r}, \mathbf{k})$, the number of particles at time t in the volume $\mathrm{d}^3\mathbf{r}$ around $\mathbf{r}$ within a $\mathrm{d}^3\mathbf{k}$ volume around $\mathbf{k}$ is given by:

$$\mathrm{d}N = f(t, \mathbf{r}, \mathbf{k})\, \mathrm{d}^3\mathbf{r}\, \mathrm{d}^3\mathbf{k}. \tag{2.17}$$

Phonons are unaffected by external fields, so the BTE assumes the following form [9]

$$\frac{\partial f}{\partial t} + \mathbf{v}_{\mathrm{g}} \cdot \nabla f = \left[\frac{\partial f}{\partial t}\right]_{\mathrm{scatt}}. \tag{2.18}$$

The left-hand side of Eq. 2.18 represents ballistic movement and causes deviations from equilibrium, while the scattering term on the right-hand side restores equilibrium due to collisions of phonons with phonons or boundaries.

The collision term is given by

$$\left[\frac{\partial f}{\partial t}\right]_{\mathrm{scatt}} = \sum_{\mathbf{k}'}[\Phi(\mathbf{k},\mathbf{k}')f(\mathbf{k}') - \Phi(\mathbf{k}',\mathbf{k})f(\mathbf{k})], \tag{2.19}$$

with $\Phi(\mathbf{k},\mathbf{k}')$ being the scattering rate from state $\mathbf{k}'$ to $\mathbf{k}$. Scattering of phonons due to the anharmonic terms of the potential (three-phonon processes) are difficult to treat, because the scattering rates are usually nonlinear functions of $\mathbf{k}$. This renders the deterministic solution of the BTE extremely difficult. However we know that three-phonon processes tend to restore thermal equilibrium. Therefore, we use the relaxation time approximation for the three-phonon scattering processes in which the distribution function $f(t,\mathbf{r},\mathbf{k})$ relaxes to an equilibrium function $f^0(\mathbf{r},\mathbf{k})$ at the rate $1/\tau$:

$$\left[\frac{\partial f}{\partial t}\right]_{scatt} = -\frac{f - f^0}{\tau}. \tag{2.20}$$

This implies that in a non-equilibrium system, the inelastic scattering term restores equilibrium following an exponential decay $f - f_0 \propto \exp(-t/\tau)$. With this approximation the BTE becomes linear.

2.4 Monte Carlo method

The Monte Carlo (MC) technique has been widely used to solve transport equations for electrons [6] and phonons [4], [5]. In an arbitrary geometry the BTE is difficult to solve in a deterministic approach, because the number of independent variables is very large. The large number of variables puts high requirements on memory and CPU capacities. The main advantage of the MC method is that these requirements are removed. Also it is possible to consider complex geometries.

In a Monte Carlo technique, the initial position $\mathbf{r}$ and momentum $\mathbf{k}$ of a particle are randomly drawn. The samples repeatedly fly and scatter after the time τ_{scatter}. Phonons move unrestrained as there is no external field. The statistics are collected at various points in time and space, and processed to extract the mean value of macroscopic variables such as the temperature field $T(\mathbf{r})$, velocity $\langle\mathbf{v}\rangle$, energy $\langle E\rangle$, or thermal conductivity κ.

2.4.1 Simulation domain and boundary conditions

It is necessary to define the geometry of the device, which is done using the GTS-Framework [17]. Among other things, the GTS-Framework contains tools for computer aided design (CAD) structure generation, meshing, circuit and device simulation and visualization of results.

Within the GTS-Framework parameters such as the device geometry and material(s) are defined and a simulation grid is created using a mesher. The mesher dissects the volume into small tetrahedra. If the tetrahedra do not conform to quality criteria, additional points are added to the mesh. The mesh may be of ortho-product or tetrahedral type. Before the simulation starts, an ortho-product mesh is decomposed to a tetrahedron mesh. Using tetrahedra instead of arbitrary polyhedra simplifies building the topology of the device. A tetrahedron has four faces, so the number of neighbours is always four. Additionally, using tetrahedra as basic cell type allows the simulation of geometric devices of arbitrary shape and complexity.

The device consists of a simulation domain and at least two thermal contacts, i.e. a heat source and a heat sink (see Fig. 2.8). Throughout the simulation the temperature of the thermal contacts is assumed to be constant: T_{source} and T_{sink}, respectively. Phonons that reach the outward boundaries of the thermal contacts are thermalized. Consequently, the contacts act as black bodies.

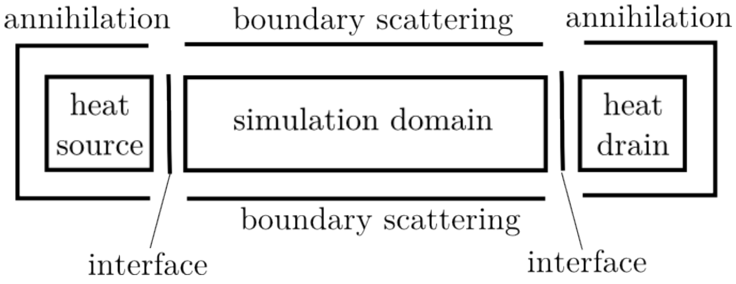

Figure 2.8: Schematic drawing of the simulation domain, the contacts and the boundary conditions in 2D.

The simulation starts by reading in the device geometry: A loop over all device segments and all grid elements is used to build spatial cells. For each cell the following geometrical information is stored: (i) coordinates of the points, which span the cell and its volume, and (ii) the normal vectors of the cells' faces and identifiers of the neighbouring cells in order to treat the transit of a phonon from one cell to another (see Fig. 2.11).

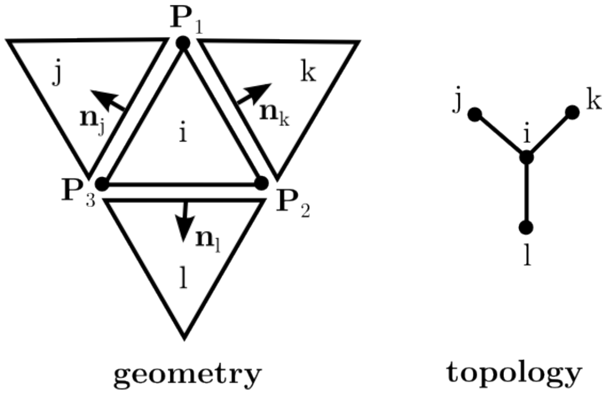

Figure 2.9: Schematic drawing of cells and their topology in 2D.

2.4.2 Simulation scheme

In principle there are two kinds of particle MC schemes: single-particle or multi-particle [4], [5]. In the first case the statistics are accumulated by repetition of the simulation sequence with a single particle, whereas for multi-particle simulations the statistics are accumulated by using a large number of particles at the same time. The main disadvantage of the multi-particle scheme is that it requires a lot of memory, which is why we use the single-particle approach. The simulations follow this scheme (see Fig.2.10):

- A phonon is initialized at a random position in the device.
- The phonon alternates between free flight and scattering events.
- In case of three-phonon scattering the energy of the phonon is reset, which violates energy conservation. Therefore, the energy of the cell is modified by $\Delta E_{\mathrm{phonon}}$. The temperature of the cell is recalculated by inversion of Eq. 2.23
- If the phonon reaches an outward boundary of the thermal contacts it is absorbed and the simulation continues with a newly created phonon.

- This sequence is repeated until the cell temperature difference between iterations is below the error tolerance of ϵ or the maximum number of iterations is reached.

- After reaching steady-state the thermal conductivity is calculated by determining the heat flux Φ. The heat flux is computed by injecting phonons from the source and the sink. Φ is then given by the net energy over the average time-of-flight (TOF) through the device.

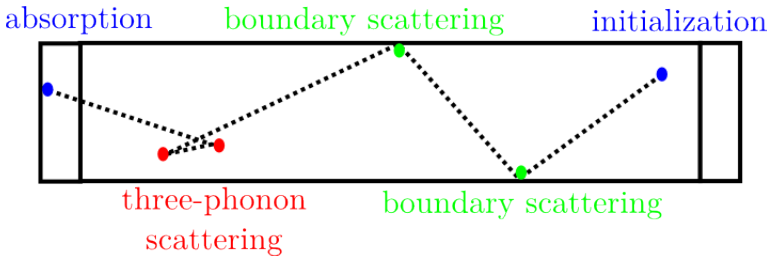

Figure 2.10: Simulation scheme for one phonon.

2.4.3 Initialization

Cell

The temperature of the thermal contacts is initialized to T_{source} and T_{sink}. Throughout the simulation the contact temperatures are assumed to be constant. The initial cell temperature within the actual simulation domain is also set to T_{sink}. The number of phonons per unit volume which is given by

$$N = \sum_p \sum_i \frac{1}{\exp(\frac{\hbar\omega_i}{k_{\mathrm{B}}T}) - 1} D(\omega_i, p)\Delta\omega_i, \tag{2.21}$$

can be a very large, e.g. $N(T = 300\,\mathrm{K}) \sim 6 \times 10^{28}/\mathrm{m}^3$. Therefore, the mean cell energy is many orders of magnitude larger than a single phonon's energy and 10^{30} iterations are needed to reach steady-state. To reduce the number of simulated phonons to N^*, we introduce a scaling factor W [4],

$$W = \frac{N^*}{N}. \tag{2.22}$$

Each stochastic sample used during the simulation actually represents an ensemble of W phonons.

The initial energy of a cell is calculated using Eq. 2.8 where the integral over frequency is replaced by a discrete sum [4],

$$E = \frac{V}{W} \sum_p \sum_i \left(\frac{\hbar\omega_i}{\exp(\frac{\hbar\omega_i}{k_{\mathrm{B}}T}) - 1} \right) g_p \frac{k^2}{2\pi^2 v_{\mathrm{g},i}} \Delta\omega_i. \tag{2.23}$$

Phonon

Cell. As there is only one phonon simulated at time, we need to select a cell in which the phonon is to be initialized. The number of phonons per cell increases with temperature, therefore our cell-selection scheme has to favour hot cells. We calculate the partial probability for cell i

$$p_i = \frac{\sum\limits_{k=1}^{i} T_k V_k}{\sum\limits_{k=1}^{N_{\mathrm{cells}}} T_k V_k}, \tag{2.24}$$

where T_i is the thermodynamic temperature and V_i is the volume of cell i. N_{cells} is the total number of cells. Then a random number R between zero and unity is drawn. If $p_{i-1} < R < p_i$, then the phonon belongs to the i-th cell.

Position. The position vector $\mathbf{r}$ of any point within a tetrahedron (= cell) is calculated using

$$\mathbf{r} = \mathbf{r_a} + \mathbf{b}R_1 + \mathbf{c}R_2 + \mathbf{d}R_3 \tag{2.25}$$

where $\mathbf{r_a}$ is the position vector the tetrahedron's vertex A and $\mathbf{b}$, $\mathbf{c}$, $\mathbf{d}$ are the edge-vectors to all other vertices. R_1, R_2 and R_3 are random numbers such that $\sum_i R_i < 1$.

Frequency. We use the following fit for the bulk dispersion relation under the isotropic Brillouin zone approximation [2]

$$\omega(k) = v_{\mathrm{s}} k + c k^2, \tag{2.26}$$

where k is the norm of the wave vector $k = |\mathbf{k}|$. For each of the different phonon branches, we use the following parameters:

branch	v_s $[m/s]$	c $[m^2/s]$
LA	9.01×10^3	-2×10^{-7}
TA	5.23×10^3	-2.26×10^{-7}

Table 2.1: Fit parameters Si by Ref. [2]

These fits are a good approximation for the phonon dispersions (see Fig. 2.2) and are easily inverted to retrieve k.

We calculate the maximum frequency $\omega_{\mathrm{max}}^{\mathrm{LA}}$ using Eq. 2.26 and $k_{\mathrm{max}} = \frac{2\pi}{a}$ with lattice parameter $a = 0.543\,071\,\mathrm{nm}$. The frequency space between zero and $\omega_{\mathrm{max}}^{\mathrm{LA}}$ is discretized into N_ω spectral intervals of width $\Delta\omega = \frac{\omega_{\mathrm{max}}^{\mathrm{LA}}}{N_\omega}$.

The number of phonons in the i-th spectral interval is given by

$$N_i = \langle n(\omega_i, \mathrm{LA})\rangle g_{\mathrm{LA}} D(\omega_i, \mathrm{LA})\Delta\omega_i + \langle n(\omega_i, \mathrm{TA})\rangle g_{\mathrm{TA}} D(\omega_i, \mathrm{TA})\Delta\omega_i \quad (2.27)$$

where the equilibrium distribution is evaluated at the central frequency of the spectral interval i. In order to determine the frequency of a phonon, the normalized cumulative number density function is calculated [4]

$$F_i = \frac{\sum\limits_{k=1}^{i} N_k}{\sum\limits_{k=1}^{N_\omega} N_k}. \quad (2.28)$$

Using Eq. 2.27 N_k is computed for the temperature of the cell in which the phonon is to be initialized. A random number R is then drawn. If $F_{i-1} < R < F_i$, then the phonon belongs to the i-th spectral interval. After drawing the spectral interval, the phonon frequency is then given by

$$\omega = \omega_i + 2(R-1)\frac{\Delta\omega}{2}. \quad (2.29)$$

Here we approximate $\omega(k)$ with a piecewise linear function.

Polarization. Any phonon has to be assigned to either a LA branch or a TA branch. The probability of a phonon being LA polarized is expressed as

$$P_i(\mathrm{LA}) = \frac{N_i(\mathrm{LA})}{N_i(\mathrm{LA}) + N_i(\mathrm{TA})}, \quad (2.30)$$

where i is the spectral interval in which the phonon belongs to. Next, a random number between zero and unity is drawn. If the random number is less than $P_i(LA)$ the phonon belongs to the LA branch. Otherwise it belongs to a TA branch.

Wave Vector. Once the phonon frequency has been sampled, the norm of the wave vector k can be determined directly by inversion of the dispersion relationship. The direction of the wave vector is given by

$$\hat{\mathbf{k}} = \begin{pmatrix} \sin\theta\cos\psi \\ \sin\theta\sin\psi \\ \cos\theta \end{pmatrix}, \tag{2.31}$$

where $\psi = 2\pi R_2$, $\cos\theta = 2R_1 - 1$, and R_1 and R_2 are random numbers between zero and unity. The wave vector is then given by

$$\mathbf{k} = k\hat{\mathbf{k}}. \tag{2.32}$$

Group Velocity. The group velocity is defined as the slope of the dispersion relation. Using the quadratic fit for the dispersion relation (Eq. 2.26) the group velocity then is

$$v_\mathrm{g} = v_\mathrm{s} + 2ck \tag{2.33}$$

and is co-directional with the wave vector $\mathbf{k}$.

Cell
index
points
neighbors
normals
facePoints
isContact
segmentIndex
volume
temperature
meanEnergy

Phonon
omega
waveVector
position
velocity
polarization
frequencyInterval

Figure 2.11: Data structure of cells and phonons.

2.4.4 Free flight

The events occurring within a time step Δt are split into two sequential phases, free flight and scattering. In the single-particle simulation we employ the time step is not required, but useful for numeric stability. However it increases the computation time. During the free flight phase, phonons move linearly in time because there is no accelerating field. The position of a phonon is given by the first-order time integration:

$$\mathbf{r}(t+\Delta t) = \mathbf{r}(t) + \mathbf{v}_{\mathrm{g}}\Delta t. \tag{2.34}$$

Following the free flight phase, if the phonon moves to a new cell, the phonon energy increases the cell energy by $\Delta E_{\mathrm{cell}} = \hbar\omega$ and the local temperature of the cell. We compute the temperature $\tilde{T}$ of the cell by a numerical inversion (Newton-Raphson method) of Eq. 2.23.

During the free flight a phonon might change cell. The time till the phonon crosses the faces of the cell is given by

$$t_i = \frac{\mathbf{d}_i - (\hat{\mathbf{n}}_i \cdot \mathbf{r})}{(\mathbf{v}_{\mathrm{g}} \cdot \hat{\mathbf{n}}_i)} \tag{2.35}$$

with $\hat{\mathbf{n}}_i$ being the normal vector of face i, and $\mathbf{d}_i$ is the position vector of a point on this face. The face which is crossed next is the one with the smallest t_i, $\tau_{\mathrm{cell}} = \min(t_i)$.

If $\tau_{\mathrm{cell}} < \Delta t$ (see Fig. 2.12) the position of the phonon is calculated using

$$\mathbf{r}(t+\Delta t) = \mathbf{r}(t) + \mathbf{v}_{\mathrm{g}}\tau_{\mathrm{cell}}. \tag{2.36}$$

Afterwards, either boundary scattering occurs, or the phonon moves to another cell. Moving to another cell is a form of self-scattering, which is not scattering due to a physical process but due to the cellular nature of the simulation volume.

2.4.5 Scattering

In this section we describe boundary and three-phonon scattering processes.

Boundary scattering. Boundary scattering does not change the phonon frequency, but solely its direction, and is significant at low temperatures where the phonon mean free path is large. Boundary scattering can be

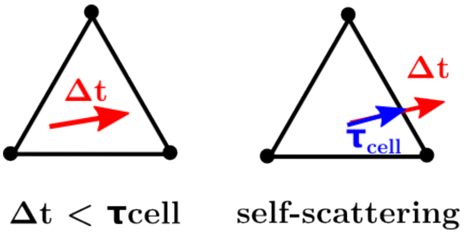

Figure 2.12: If the timestep Δt is smaller than the time till the phonon crosses the next face of the cell τ_{cell} the phonon remains in this cell. Otherwise, self-scattering or boundary scattering occurs.

treated phenomenologically by introducing a relaxation rate $\frac{1}{\tau_B} \propto \frac{1}{D}$ where D is the dimension of the system. In our simulations boundary scattering is an actual interaction of a phonon with the geometric boundary of the device. A phonon can be specularly reflected using the relation

$$\mathbf{v}_{\text{r}} = \mathbf{v}_{\text{i}} - 2(\mathbf{v}_{\text{i}} \cdot \hat{\mathbf{n}})\hat{\mathbf{n}} \tag{2.37}$$

where $\mathbf{v}_{\text{i}}$ is the incident, $\mathbf{v}_{\text{r}}$ is the reflected phonon velocity, and $\hat{\mathbf{n}}$ is the normal vector on the boundary face.

Only perfectly smooth surfaces reflect phonons specularly. In order to implement surface roughness we introduce a specularity parameter p,

$$p = \begin{cases} 0 & \text{completely diffuse} \\ 1 & \text{specular} \end{cases} \tag{2.38}$$

For every surface scattering event a random number R is drawn. If $R > p$ the phonon is scattered diffusely, which involves resetting its direction vector as:

$$\hat{\mathbf{v}}_{\text{r}} = \hat{\mathbf{t}}_1 \sin\theta\cos\psi + \hat{\mathbf{t}}_2 \sin\theta\sin\psi - \hat{\mathbf{n}}|\cos\theta|. \tag{2.39}$$

Here θ and ψ are random angles which are calculated as described in Sec. 2.4.3, $\hat{\mathbf{t}}_1$ and $\hat{\mathbf{t}}_2$ are the tangents, and $\hat{\mathbf{n}}$ is the normal vector on the face. For intermediate values of the specularity parameter, e.g. $p = 0.1$ the phonons are scattered diffusely in 90% of the boundary scattering events. For comparison between specular and diffusive scattering see Fig. 2.13

The probability whether a phonon scatters specularly also depends on the phonon's wave vector. The specularity probability is given by [3]

$$p(k) = \exp(-4k^2 n_{\text{r}}^2), \tag{2.40}$$

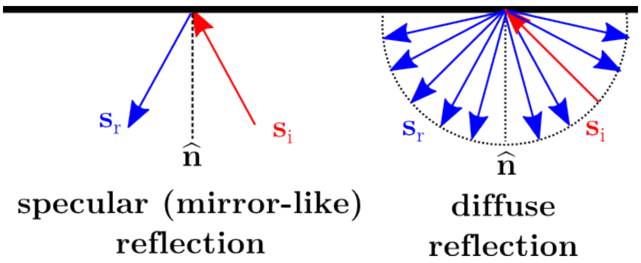

Figure 2.13: Phonon reflection at the boundary.

with n_r being the RMS value of the boundary roughness. It is possible to simulate devices with either a constant specularity parameter p, or a given roughness n_r.

Three-phonon scattering. During any three-phonon process, energy and momentum conservation must both be satisfied simultaneously. In principle, in a multi-particle simulation, it is possible to incorporate three-phonon scattering by treating each phonon as a potential candidate for scattering and allowing it to interact with every other phonon in its vicinity. Energy and momentum conservation would then decide, if an interaction between phonons is possible. In this work only one phonon is simulated at a time. Even for multi-particle simulations such computations would be too expensive for practical problems. The problem is addressed using perturbation theory. The equilibrium distribution is perturbed and all third-order interactions are considered at a given temperature, allowing the system to come back to equilibrium. The final outcome of such analysis are expressions for phonon lifetimes as functions of frequency ω and temperature T for both polarization branches [7]:

$$\tau_\mathrm{LA}^{-1} = B_\mathrm{NU}^\mathrm{LA}\omega^2 T^3 \tag{2.41}$$

$$\tau_\mathrm{TA,N}^{-1} = B_N^\mathrm{TA}\omega T^4 \tag{2.42}$$

$$\tau_\mathrm{TA,U}^{-1} = \begin{cases} 0 & \omega < \omega_{1/2} \\ B_\mathrm{U}^\mathrm{TA}\omega^2 \sinh\left(\frac{\hbar\omega}{k_\mathrm{B}T}\right) & \omega \geq \omega_{1/2} \end{cases} \tag{2.43}$$

$$\tag{2.44}$$

$\omega_{1/2}$ is the frequency corresponding to $k = k_\mathrm{max}/2$. This frequency limit $\omega_{1/2}$ is a choice which represents the fact that low-frequency phonons seldom occur in processes in which the sum of the wave vectors is larger than the reciprocal lattice vector **G**, which is the condition for U processes (see Fig. 2.5). We are only able to trace one phonon at a time. If the traced phonon has a large wave vector (i.e. $k > k_{\max}/2$) then is is likely to undergo an Umklapp process with a thermal phonon (i.e. $k < k_{\max}/2$). The time-scale, τ_{NU} , is an effective time-scale which accounts for both normal (N) and Umklapp (U) processes using the Matthiessen rule

$$\tau_{\mathrm{NU}}^{-1} = \tau_{\mathrm{N}}^{-1} + \tau_{\mathrm{U}}^{-1}. \tag{2.45}$$

Normal scattering does not contribute to thermal resistance. Here the energy of the phonon is modified which can affect wave-vector dependent surface scattering of Eq. 2.40.

constant	value
$B_{\mathrm{NU}}^{\mathrm{LA}}$	2×10^{-24}
$B_{\mathrm{N}}^{\mathrm{TA}}$	9.3×10^{-13}
$B_{\mathrm{U}}^{\mathrm{TA}}$	5.5×10^{-18}
$\omega_{1/2}$	4.7×10^{13}

Table 2.2: Parameters for τ_{NU} in Si [7]

The three-phonon scattering processes are implemented in the following manner. First, a phonon's effective lifetime τ_{NU} is calculated using Eq. 2.44 and the local temperature of the cell $\tilde{T}$. The scattering probability is given by

$$P_{\mathrm{NU}} = 1 - \exp(-\Delta t/\tau_{\mathrm{NU}}). \tag{2.46}$$

Next, a random number is drawn and compared with P_{NU}. If the random number is less than P_{NU}, the phonon is scattered. Scattering is implemented by resampling the phonon's frequency, wave vector, and group velocity. The resetting of the frequency is done in a similar fashion as in the initialization scheme. However, we need to make sure that energy is conserved and phonons are created at the same rate as they are destroyed (Kirchhoff law). Therefore, we use a slightly modified distribution function [5],

$$F_{i,\mathrm{scatt}} = \frac{\sum\limits_{j=1}^{i} N_j(\tilde{T}) P_{\mathrm{NU}}(\omega_j)}{\sum\limits_{j=1}^{N_\omega} N_j(\tilde{T}) P_{\mathrm{NU}}(\omega_j)}. \tag{2.47}$$

Taking into account the scattering probability in the distribution function F_{scatt} ensures that a phonon is resampled with not too weak energy as it can be seen in Fig. 2.14. Here we compare the distribution function with (F_{scatt}) and without scattering probability modification (F as defined in Eq. 2.28) as a function of the frequency for temperatures 300 K and 500 K. For $T \leq 300\,\text{K}$ and $\omega < 3 \times 10^{13}\,\text{s}^{-1}$, F_{scatt} is lower than F. Therefore, by using the scattering probability modification phonons are resampled with larger energies than without this modification. For 500 K, F_{scatt} and F are almost equal, which reflects the fact that for large temperatures the scattering probability $P_{\text{NU}} \sim 1$ for all frequency intervals.

Since we are only able to trace one phonon at a time, momentum conservation can not be rigorously treated. To correct this, we use the following procedure to take into account the fact that Umklapp processes contribute to the thermal resistance, whereas the normal processes do not. When phonons scatter through U processes, their directions after scattering are randomly chosen as is done in the initialization procedure. For N processes, phonons do not change their propagation direction but only their frequency [7], [5].

The relaxation time approximation [7] states that there is a frequency limit $\omega_{1/2}$ for TA-phonons. Umklapp processes only occur above this frequency. On the other hand, normal processes are only considered for $\omega < \omega_{1/2}$ and the propagation direction must be resampled. For the longitudinal branch there is no frequency limit and according to Ref. [7], only N processes exist. Therefore, momentum has to be conserved for each scattering event involving a LA phonon. Ref. [5] states that this leads to thermal conductivity values higher than the measured ones for temperatures between 100 K and 250 K. More realistic results were obtained by resetting the direction of LA-phonons for half the collisions, which is also done in this work.

Resetting the state of the phonon essentially thermalizes the phonon and helps restore equilibrium, which is the most important function of three-phonon scattering processes in the simulation. When the frequency of a phonon is changed, energy conservation is violated. To correct this, the energy of the cell is modified,

$$E_{\text{cell}} \rightarrow E_{\text{cell}} + \hbar \Delta\omega. \tag{2.48}$$

The new temperature of the cell is calculated by inversion of Eq. 2.23 using the Newton-Raphson method.

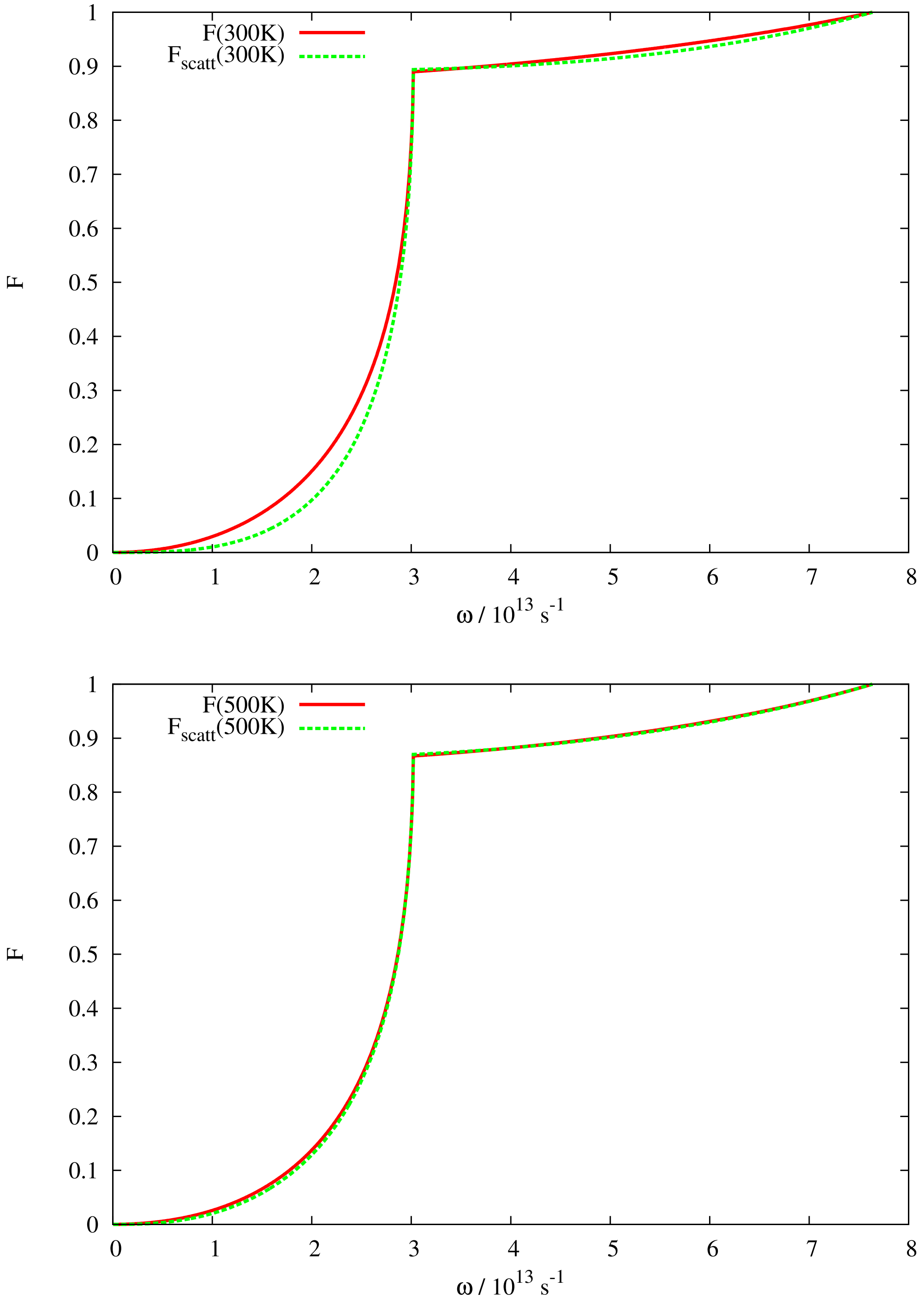

Figure 2.14: Normalized number density function for Si at $T = 300\,\mathrm{K}$ (top) and $T = 500\,\mathrm{K}$ (bottom), with and without P_{NU} correction.

2.4.6 Thermal conductivity

The phonon free flight and scattering processes are iterated until steady-state is reached. The number of iterations depends on the size of the device and the time step Δt. The simulation outputs at this step are the position-dependent temperature $T(\mathbf{r})$ and cell energy $E(\mathbf{r})$.

Afterwards the thermal conductivity is calculated using the heat flux Φ through the medium for a given thermal gradient ∇T by applying Fourier's law. For a simple cuboid device with length $L_\mathrm{z} = L$, cross sectional area A and temperature difference ΔT between $L_\mathrm{z} = 0$ and $L_\mathrm{z} = L$, the thermal conductivity is given by

$$\kappa = \frac{1}{A}\frac{L}{\Delta T}\Phi. \tag{2.49}$$

To calculate the phonon heat flux, we sequentially inject a prescribed number N_p of phonons first from $L_\mathrm{z} = 0$ into the device. We sum the phonons' incident energy to

$$E_0^\mathrm{in} = \sum_{i=0}^{N_\mathrm{p}} \hbar\omega_i. \tag{2.50}$$

As the phonons travel through the device, they engage in three-phonon scattering which might alter their frequency and direction of movement. The energy of all back-scattered phonons (leaving the device at $L_\mathrm{z} = 0$) is summed up to E_0^out. Additionally, we calculate the average time that it takes for a phonon to travel the distance through the device $\langle\mathrm{TOF}\rangle$. The TOF of a phonon is given by sum of all free flight and scattering times.

Then we repeat the procedure, but now we initialize the phonons from the cold side at $L_\mathrm{z} = L$ and calculate E_L^{in} and E_L^{out}. Because of the temperature difference between both device ends, the energy of the phonons injected at $L_\mathrm{z} = L$ is modified by a factor of $s = \frac{N(T(L))}{N(T(0))}$. The phonon flux is then given by

$$\Phi = N_\mathrm{tot}\frac{(E_0^\mathrm{in} - E_0^\mathrm{out}) - s(E_\mathrm{L}^\mathrm{in} - E_\mathrm{L}^\mathrm{out})}{N_\mathrm{p}\langle\mathrm{TOF}\ \rangle}, \tag{2.51}$$

where N_tot is the total number of phonons inside the device and N_p is the number of prescribed phonons. N_tot is calculated using Eq. 2.21 for all cells. Fig. 2.15 visualizes the simulation scheme for calculating the flux. This scheme can also be applied to calculate the flux between cells.

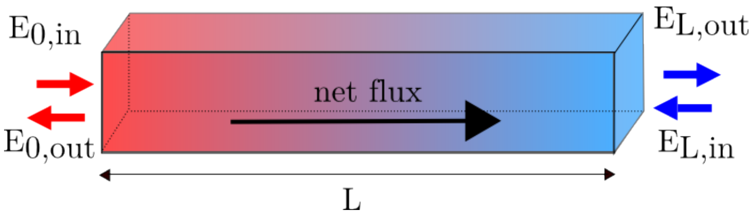

Figure 2.15: Simulation scheme for calculating the heat flux Φ of a cuboid shaped device. The temperature difference between the ends of the device is indicated by the color gradient with red symbolizing hot. $E_{\mathrm{i}}^{\mathrm{in}}$ and $E_{\mathrm{i}}^{\mathrm{out}}$ are sums of energies of phonons that are injected and extracted, respectively.

Chapter 3

Results

3.1 Time-of-flight (TOF) simulations

In this section we investigate the TOF of phonons depending on geometric aspects of the device such as lengths or surface roughness and neglect phonon-scattering. We are restricting the calculations to this limit, because we want to be able to distinguish properties that arise from the system's geometry from the effects that arise due to phonon scattering.

The three-phonon scattering will be included in the next section to calculate the thermal conductivity. The thermal conductivity is a more complex quantity, however it is roughly inversely proportional to the TOF.

3.1.1 Constant specularity, square cross sectional area

Here, we investigate the TOF for cuboid-shaped Si devices with a square-shaped cross sectional area. In Fig. 3.1 we plot the TOF as a function of the frequency ω for LA and TA phonons separately for a device with dimensions $30 \times 30 \times 1000\,\text{nm}$. We calculate the TOF for several values of the specularity parameter $p = \{0.1, 0.25, 0.5, 0.75, 1.0\}$ with $p = 1$ being fully specular and $p = 0$ being diffuse boundary scattering. We find that the TOF increases with the frequency which is due to to the decrease in group velocity (see Fig. 2.4). Especially TA phonons display this distinct tendency (see Fig. 3.1b), because the decrease in group velocity is larger for the TA branch than for the LA branch. Upon increasing the specularity parameter the TOF decreases throughout the spectrum. This is expected, since in the diffusive limit phonons are reflected into arbitrary directions from the device surface. In case of diffusive scattering it is possible that the direction of propagation of a phonon is reversed with respect to the heat flow. Therefore, phonons can scatter back and forth inside the device, and hence the TOF is longest in the diffusive limit. At larger specularity parameter, the number of diffusely reflected phonons is reduced, leading to a decrease in the TOF.

To study systematically the effects of different cross sectional areas A, in Fig. 3.2 we plot the ratio TOF/A over the frequency ω with specularity parameter $p = 0.5$ and constant length $L_\mathrm{z} = 1\,\mu\mathrm{m}$. The most important effect occurs between $A = 30 \times 30\,\mathrm{nm}^2$ and $A = 100 \times 100\,\mathrm{nm}^2$. For $30 \times 30\,\mathrm{nm}^2$ the TOF is distinctively larger for the whole frequency range, than it is for $100 \times 100\,\mathrm{nm}^2$. On further increase of the cross sectional area the TOF stays almost constant. With increasing values of the cross sectional area, phonons gradually scatter less at the surface. Therefore, diffusive surface scattering plays a much more decisive role for small cross sectional areas. Is seems, however, that the strongest effect of boundary scattering happens for dimensions below 100 nm as also observed in experiments with nanowires of similar cross sections [16].

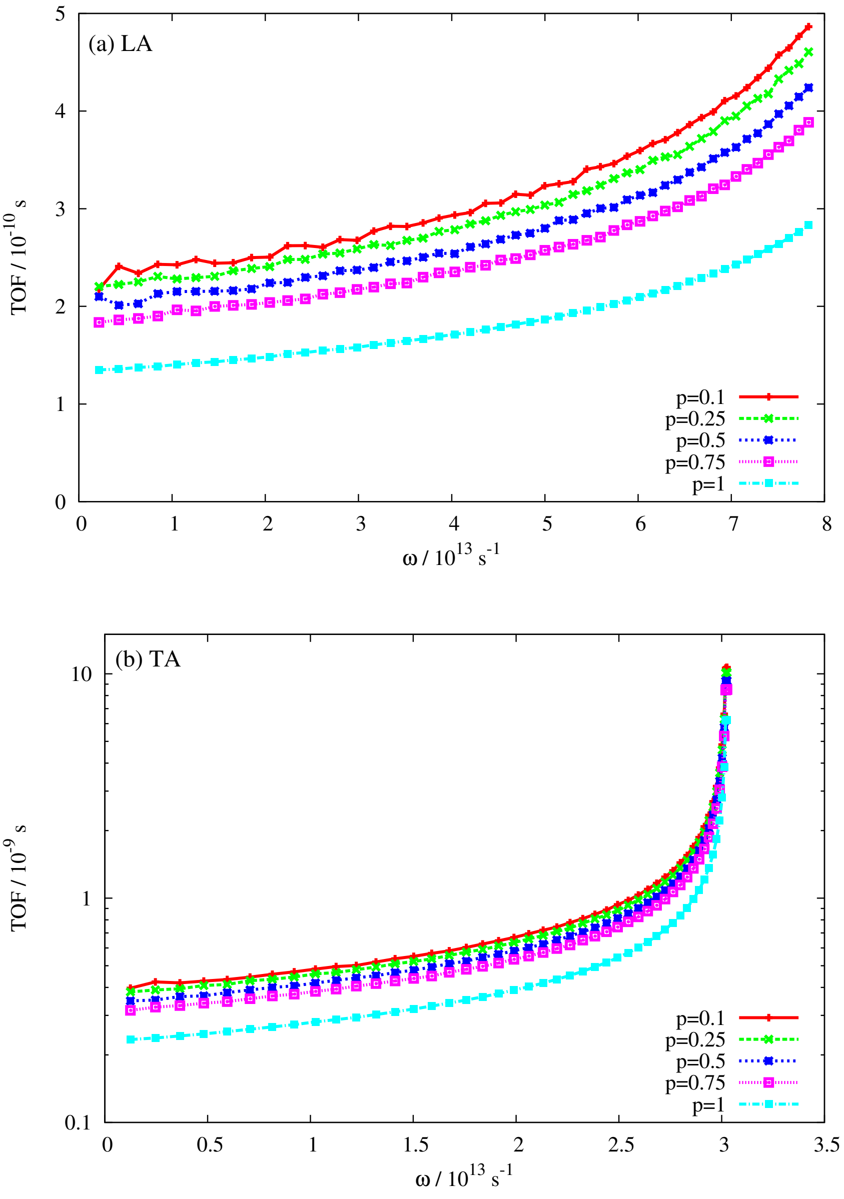

Figure 3.1: TOF(ω) for a $30 \times 30 \times 1000$ nm device for LA (a) and TA (b) phonons at $p = \{0.1, 0.25, 0.5, 0.75, 1.0\}$. Upon decrease of the specularity parameter p the TOF increases.

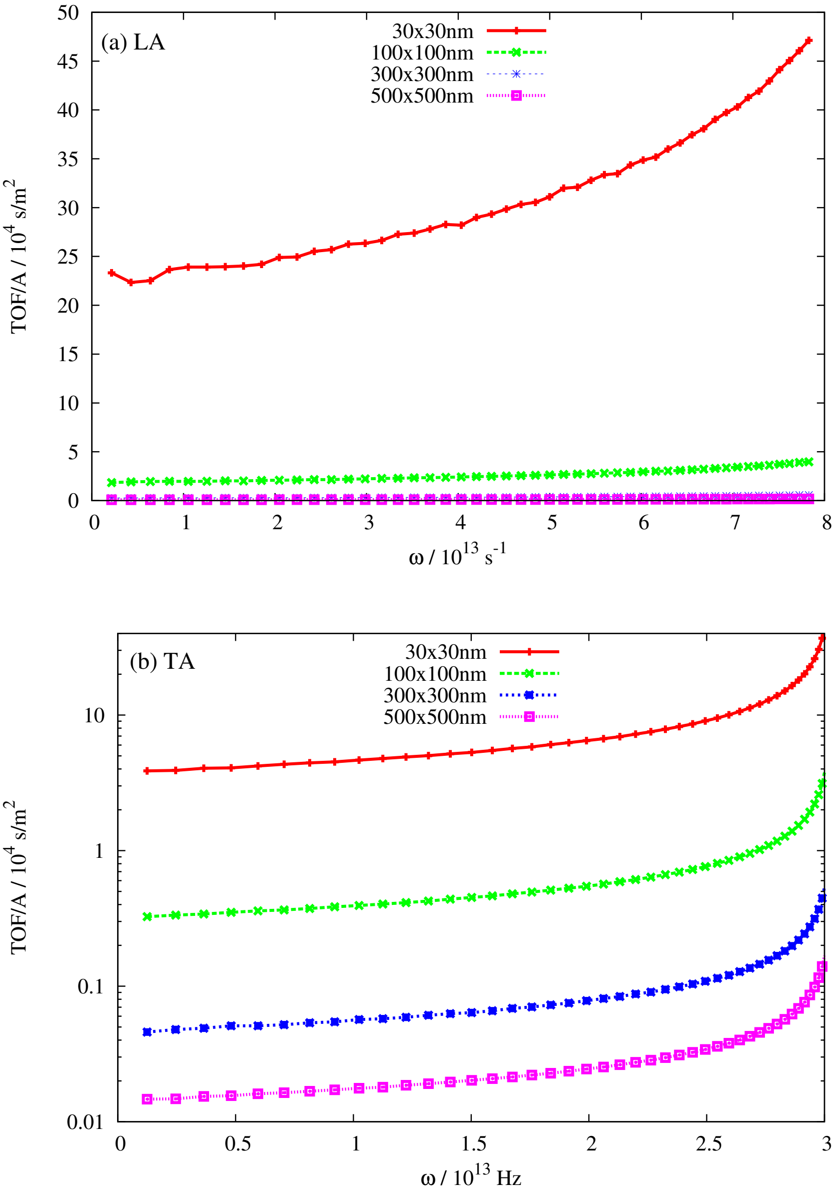

Figure 3.2: TOF(ω)/A, where A is the cross sectional area for LA (a) and TA (b) phonons and $p = 0.5$. For $A = 30 \times 30\,\mathrm{nm}^2$ the TOF/A is distinctively larger throughout the spectrum, whereas for $A = 100 \times 100\,\mathrm{nm}^2$ the TOF/A is lower and almost constant on further increasing A.

3.1.2 Constant specularity, non-square cross sectional area

We observed a decrease in TOF with cross section area A for devices with square cross sections. It is interesting, however, to calculate the TOF for more general, i.e. non-square-shaped, devices with large aspect ratios. In this way we can understand which surface parts cause TOF increase, and relate our results to thermal conductivities of thin layers.

We consider a device with dimensions $L_{\mathrm{z}} = 1\,\mu\mathrm{m}$ (length) and $L_{\mathrm{y}} = 30\,\mathrm{nm}$ (height). The width L_{x} of the device is gradually increased from 30 nm to 1 µm. In Fig. 3.3, we show the evolution of the TOF with L_{x} for various values of the specularity parameter for the maximum frequency of the respective branch ω_{max}. We choose this frequency, because our previous results suggest that the difference between the TOF for various values of the specularity parameter is most pronounced here. We find a decrease of the TOF with L_{x} up to 500 nm, whereas the TOF is almost constant upon further increase of the width. For large values of width L_{x}, the number of boundary scattering events is reduced and the TOF becomes independent of L_{x} (bulk-like). Similarly to the square-shaped cross sectional devices, the specularity parameter has more impact on the TOF of devices with small A. It seems, therefore, that for feature sizes above 500 nm, the effect of the boundary is negligible.

3.1.3 Constant vs non-constant specularity

In Fig. 3.4 we compare the TOF in devices with boundaries of constant specularity parameter p, to the TOF of devices with boundaries that have k-dependent specular scattering probability as in Eq. 2.40. The dimensions of the device are $30 \times 30 \times 1000\,\mathrm{nm}$. The RMS value of the surface roughness $n = 0.3\,\mathrm{nm}$ corresponds best to real Si surfaces and matches approximately the $p = 0.1$ results, except for small frequencies. Analyzing Eq. 2.40 we see that the specularity probability approaches unity with the wave vector and the frequency going to zero. Here, the wave length λ of the phonons is large in comparison with the surface roughness, which leads to more specular scattering and a decrease in the TOF. In contrast to that, we observe no such reduction in the TOF(ω) curve for $n = 3\,\mathrm{nm}$. Here, the large value of the surface roughness results in diffusive scattering throughout the spectrum.

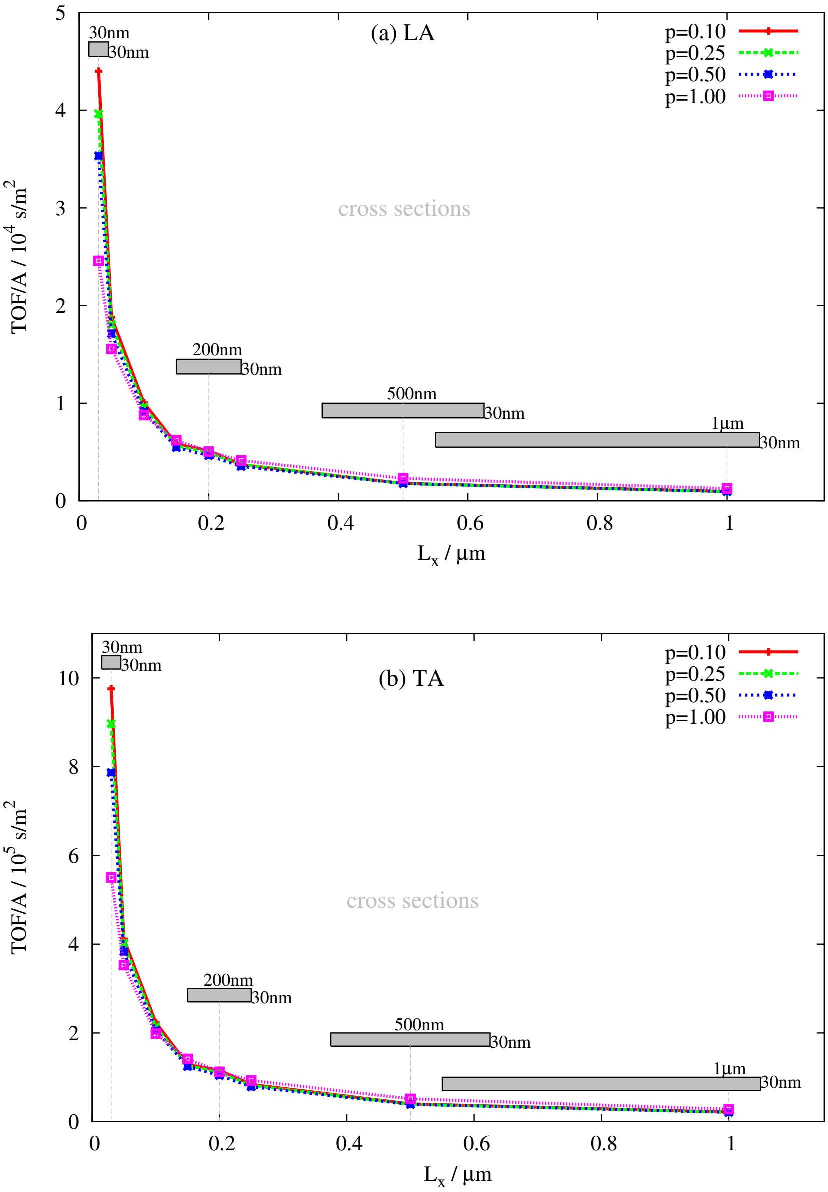

Figure 3.3: TOF for ω_{max} over device width L_{x} for LA (top) and TA phonons (bottom) with $p = \{0.1, 0.25, 0.5, 0.75, 1.0\}$, $L_{\mathrm{z}} = 1\,\mu\mathrm{m}$ and $L_{\mathrm{y}} = 30\,\mathrm{nm}$. The gray rectangles indicate the cross sections. For $L_{\mathrm{x}} < 500\,\mathrm{nm}$ the TOF decreases upon increase of the device width, while the TOF becomes independent of L_{x} for $L_{\mathrm{x}} \leq 500\,\mathrm{nm}$. The specularity parameter has much more impact on devices of small width and, therefore, small cross sectional areas.

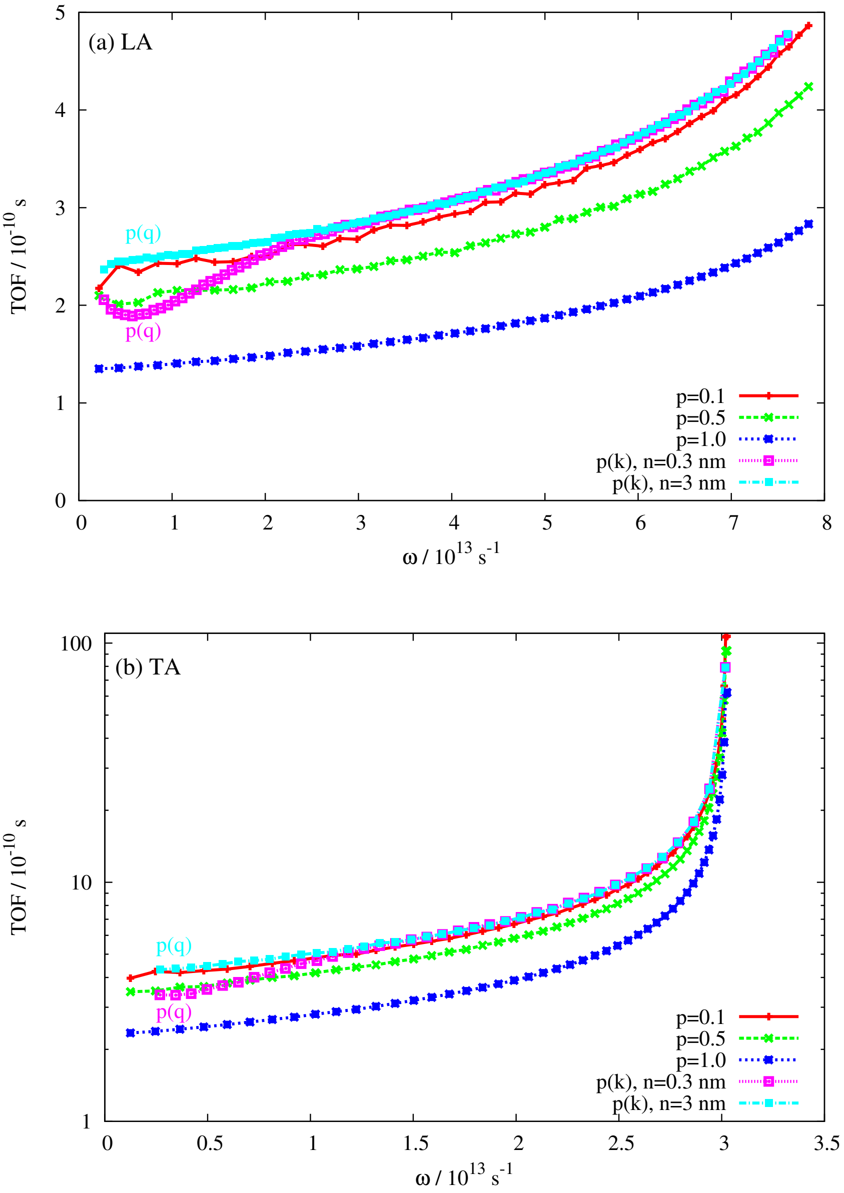

Figure 3.4: TOF(ω) for a $30 \times 30 \times 1000$ nm device for LA (top) and TA (bottom) phonons with constant specularity parameter $p = \{0.1,\ 0.5,\ 1\}$ or specularity probability with surface roughness $n = \{0.3,\ 3\}$ nm. Due to the k-dependence of the TOF for $n = 0.3$ nm, the results for low ω are in accordance with $p = 0.5$, whereas for large ω, the curve matches $p = 0.1$ better. Contrary to that, the curve for $n = 3$ nm approximately fits $p = 0.1$ for all frequencies.

3.2 Including three-phonon scattering

In the following, we present the results obtained including three-phonon scattering. To assess the simulation method we calculate temperature distributions of the device for different temperature gradients and analyze phonon trajectories. Then we perform thermal conductivity simulations for pure bulk Si and compare the results to experimental data. Finally, we calculate the thermal conductivity of nanoporous Si membranes at room temperature.

3.2.1 Temperature distribution and phonon trajectories

To test the code and ensure it reproduces the correct steady-state temperature distribution within the material we simulate a Si device with dimensions $500 \times 500 \times 1000\,\mathrm{nm}$. The time step Δt is $5\,\mathrm{ps}$, the temperature difference ΔT between hot and cold end of the device is set to $20\,\mathrm{K}$, the scaling factor W is 4×10^4, and the number of spectral intervals N_ω is 1000. For $T_{\mathrm{source}} = 310\,\mathrm{K}$, $T_{\mathrm{sink}} = 290\,\mathrm{K}$ and a specularity parameter $p = 1$ the temperature distribution is a linear gradient, which is indicated by the color gradient in Fig. 3.5. We also show the trajectories of some examples of phonons using thick black lines. Three-phonon scatter points are denoted by red dots.

Since reaching the steady-state distribution is a difficult and computationally expensive task we prescribe a thermal gradient for $T_{\mathrm{source}} = 60\,\mathrm{K}$ and $T_{\mathrm{sink}} = 40\,\mathrm{K}$ and compare the trajectories to the results at larger temperatures. By comparing Fig. 3.5a with Fig. 3.5b it is obvious that the number of three-phonon scattering events increases with the temperature. All depicted phonons are initialized at the source contact (right), but only a fraction of the number of initialized phonons actually reach the sink contact (left) due to Umklapp scattering. Particularly for large temperatures $T \sim 300\,\mathrm{K}$ we observe this distinctive effect. By comparing high and low temperature trajectories we also observe that surface scattering is more dominant in the low temperature regime.

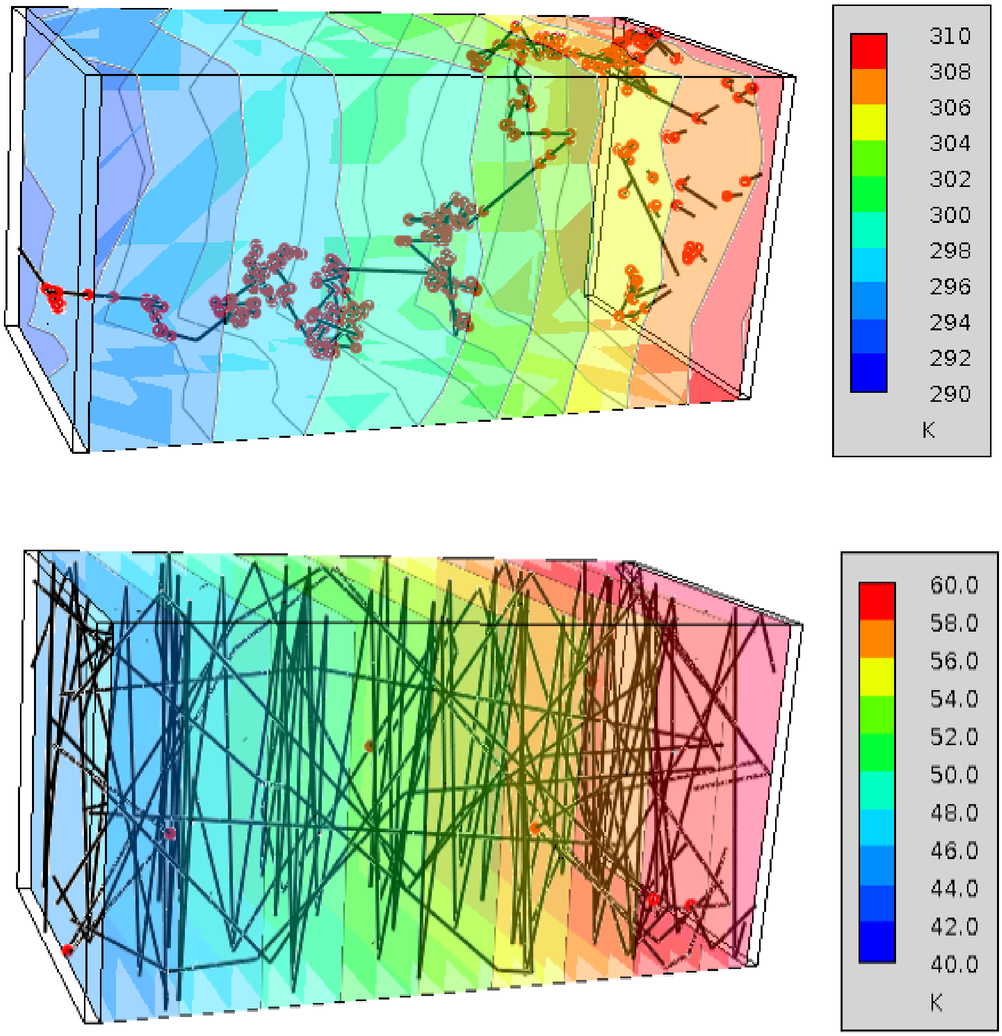

Figure 3.5: Simulated (top) and prescribed (bottom) temperature distribution for a 500 × 500 × 1000 nm Si device. The contact temperatures are $T_{\text{source}} = 310\,\text{K}$ (60 K) and $T_{\text{sink}} = 290\,\text{K}$ (40 K). The local temperature is color coded. We indicate phonon trajectories with thick black lines and three-phonon scatter points with red dots. With temperature the number of three-phonon scattering events rises, which increases the fraction of backscattered phonons.

3.2.2 Bulk Si thermal conductivity

To test the code quantitatively we calculate the thermal conductivity κ using the same parameters as previously mentioned. Instead of computing the steady-state temperature distribution, a thermal gradient is prescribed for computational efficiency. Our previous results suggest that the calculated thermal distribution is a linear gradient, which is why we prescribe this distribution. Simulations are carried out between 15 K and 300 K for a device of size $500 \times 500 \times 1000$ nm. The results are compared to measured values of Ref. [7] (see Fig. 3.6). The temperature difference between source and sink ΔT is 20 K to determine average thermal conductivities. For $T \geq 150$ K the simulation results are in agreement with measurements. However, the simulated value is below the measured one. On the other hand, in contrast to the distinct low-temperature peak that is observed in measurements, the peak in the simulated data is much lower and appears at higher temperatures ($\sim$ 120 K instead of 20 K). The reasons behind this, and the steps to calibrate the simulator further, are described below.

The peak reflects the following physical effects: For very low temperatures (from $T = 0$ K to $T = 15$ K) the thermal conductivity rises with temperature, because the number of phonons and their energies increase with T. In this regime three-phonon scattering is small. Between 15 K and 150 K the thermal conductivity declines sharply due to three-phonon processes. For temperatures larger than 150 K phonon scattering is strong, but the number of phonons is sufficiently large, such that the decline is smaller.

The deviation of measured and simulation results at low temperatures can be explained as follows: The mean free path (MFP) λ of phonons grows inversely proportional with the temperature as low $\mathbf{k}$ phonons dominate the transport. For low temperatures the mean free path λ becomes larger than the device length, which is 1 µm. To calculate the correct bulk thermal conductivity the dimensions of the device have to be much larger than λ, for phonons to scatter several times within the channel. For example at 15 K this would require the simulation of a device with a length of several mm [12]. However, this is unfeasible. According to Ref. [13] the bulk thermal conductivity can be calculated the following manner

$$\kappa_{\text{bulk}} = \kappa_{\text{L}} \frac{L + \lambda}{L}. \tag{3.1}$$

Here κ_{L} is the thermal conductivity for device with length L. Effectively the calculated thermal conductivity is scaled with the channel length, accounting for the ballisticity of the low $\mathbf{k}$ phonons in short simulation domains.

As shown in Fig. 3.7 much better agreement with measurement data is reached in the low-temperature regime using the bulk thermal conductivity κ_{bulk}. Here we also plot the results with varied ΔT such that $\Delta T = 0.05\,T_{\text{avg}}$. T_{avg} is the average temperature of the device given by $(T_{\text{source}} + T_{\text{sink}})/2$. This is done to ensure that the temperature difference is small compared to the average temperature. For $\Delta T = 0.05\,T_{\text{avg}}$, the low-temperature peak is captured the best. The reason is that in this work the relaxation time approximation is employed to simplify the Boltzmann transport equation. This approximation only holds for small deviations from the thermal equilibrium, which is why the most accurate results are achieved for small ΔT.

We finally note that achieving good match to experimental data of the thermal conductivity of bulk materials is in general non-trivial. Most studies only consider temperatures above 100 K (see the results of of Ref. [5] in Fig. 3.7).

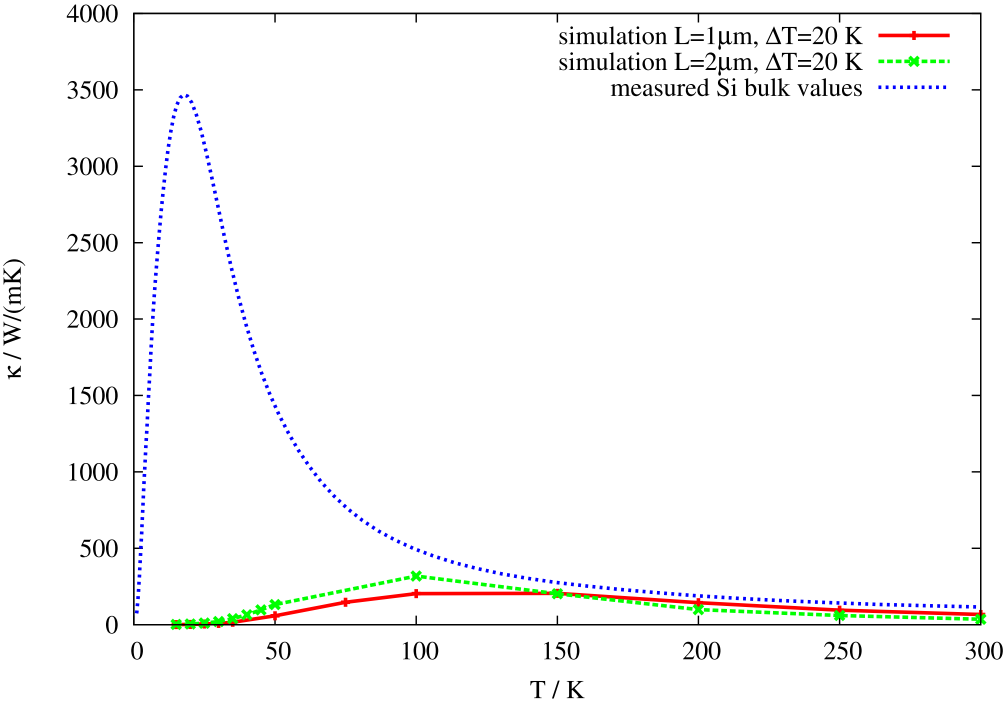

Figure 3.6: Comparison of calculated κ_{L} and measured [7] thermal conductivity. The device dimensions are $500 \times 500\,1000\,\mathrm{nm}$ and ΔT is $20\,\mathrm{K}$.

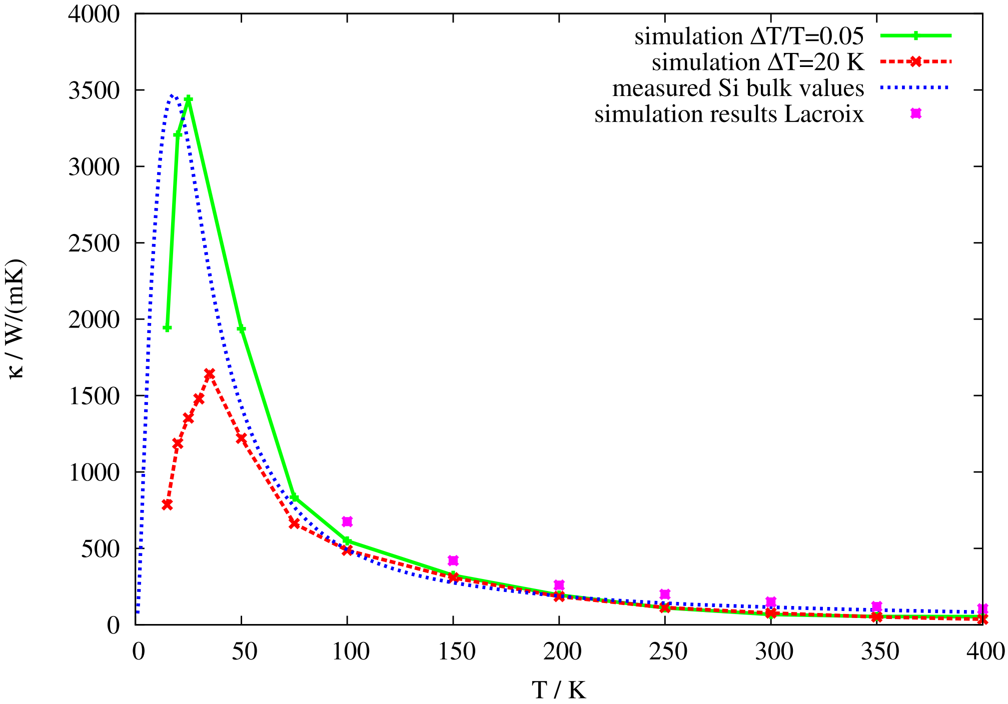

Figure 3.7: Calculated and measured [7] bulk thermal conductivity κ_{bulk}. Simulation values of Ref. [5] are plotted for comparison.

3.2.3 Si nanomeshes

In this section, we investigate the thermal properties of thin Si membranes with a high density of nanoscopic holes. For these Si nanomeshes, devices with porosity $\phi = 50\%$ and $\phi = 50\%$ are simulated. The porosity is defined by the ratio:

$$\phi = \frac{V_\mathrm{h}}{V_\mathrm{tot}}, \tag{3.2}$$

where V_h is the volume of the holes and V_tot is the total or bulk volume of the material. The hole radius is $r = 25\,\mathrm{nm}$ and the device dimensions are $500 \times 100 \times 1000\,\mathrm{nm}$ (see Fig. 3.8).

We apply a thermal gradient as indicated by the color gradient and calculate trajectories of phonons at room temperature with $\Delta T = 20\,\mathrm{K}$. In Fig. 3.9, phonon trajectories are compared for a $500 \times 100 \times 1000\,\mathrm{nm}$ device with 50% porosity for specularity parameter $p = 1.0$ and $p = 0.1$. The number of backscattered phonons decreases with increasing specularity parameter p. For low specularity parameter ($p = 0.1$) most phonons do not pass the second row of holes.

At room temperature, the thermal conductivity is calculated for different values of the specularity parameter $p = \{0.1, 0.5, 1.0\}$ (see Fig. 3.10). We find a decrease of thermal conductivity with increasing porosity ϕ and decreasing specularity parameter p.

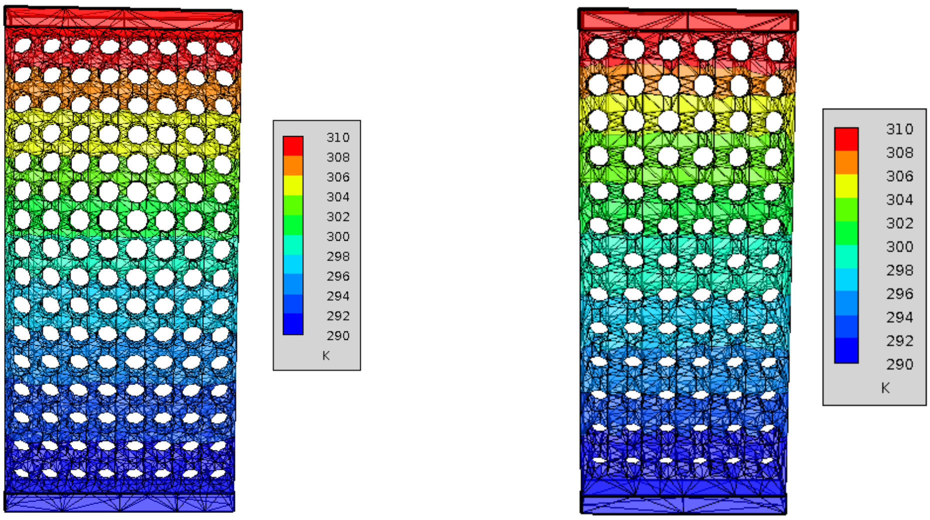

Figure 3.8: 500 × 100 × 1000 nm device with 50% porosity (left) and 35% porosity (right). The prescribed temperature distribution is indicated by the color gradient. Thin black lines represent the simulation grid.

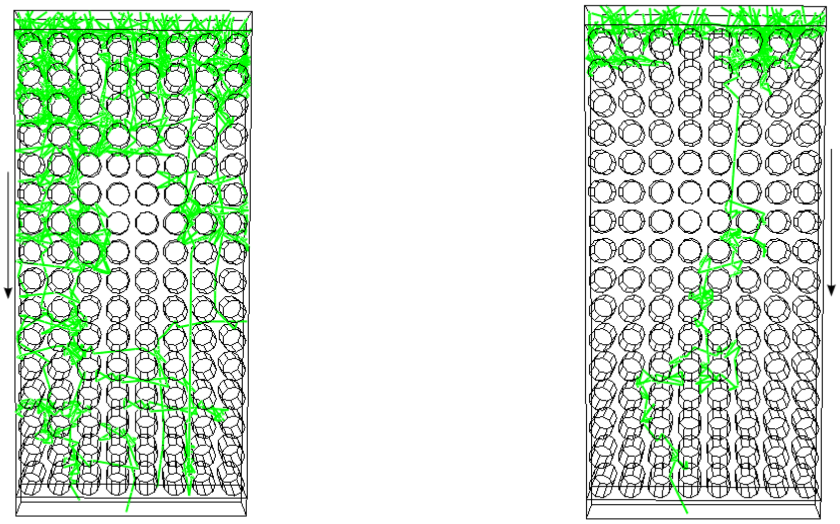

Figure 3.9: Phonon trajectories (green lines) in a 500 × 100 × 1000 nm device with 50% porosity for specularity parameter $p = 1.0$ (left) and $p = 0.1$ (right). The arrows indicate the direction of the flow.

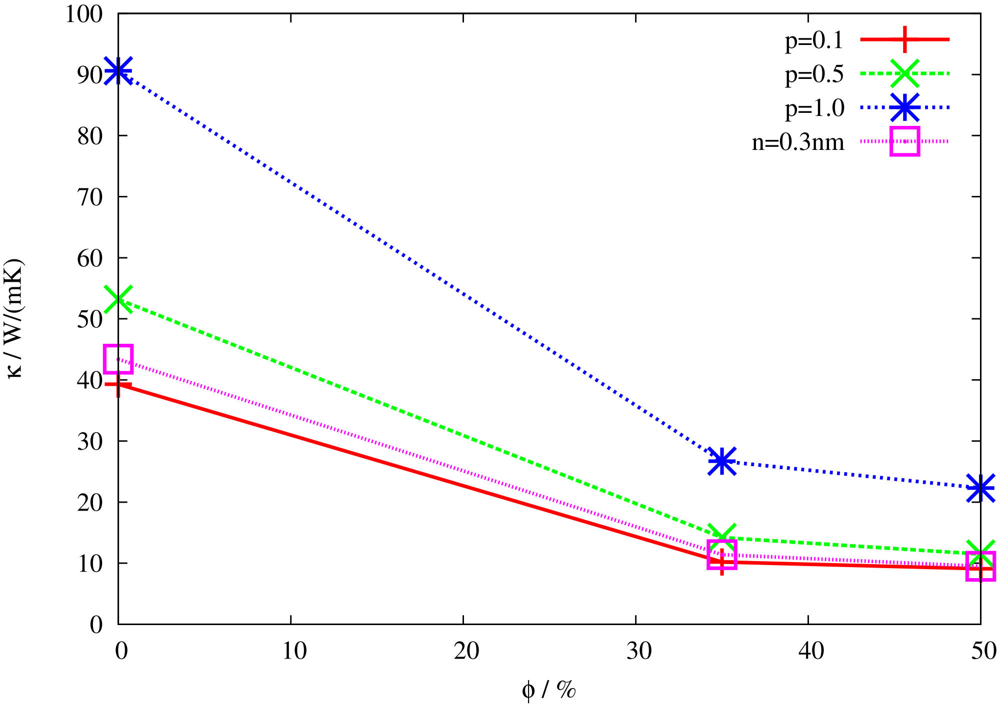

Figure 3.10: Thermal conductivity of the Si nanomesh over porosity ϕ for specularity parameter $p = \{0.1,\ 0.5,\ 1.0\}$ or surface roughness $n_\mathrm{r} = 0.3\,\mathrm{nm}$.

In experiments a different arrangement of the holes was used. Therefore, we analyze devices using a hexagonal arrangement of the holes (see Fig. 3.11), which is expected to lower the thermal conductivity. Trajectories of phonons depending on the specularity parameter are shown in Fig. 3.12.

The thermal conductivity at room temperature is calculated and the two hole arrangements are compared to measurement data in Fig. 3.13. Since in the hexagonal set-up the holes are not aligned, phonons can not travel in straight lines and scatter more. In case of (partially) diffusive boundary scattering this reduces the thermal conductivity further compared to the previous results of the rectangular structure. The simulation results are of similar amplitude but higher than the measurement results of Ref. [14].

The reason for this discrepancy might be the existence of coherent effects in the experimental structures that lead to a further reduction of the thermal conductivity.

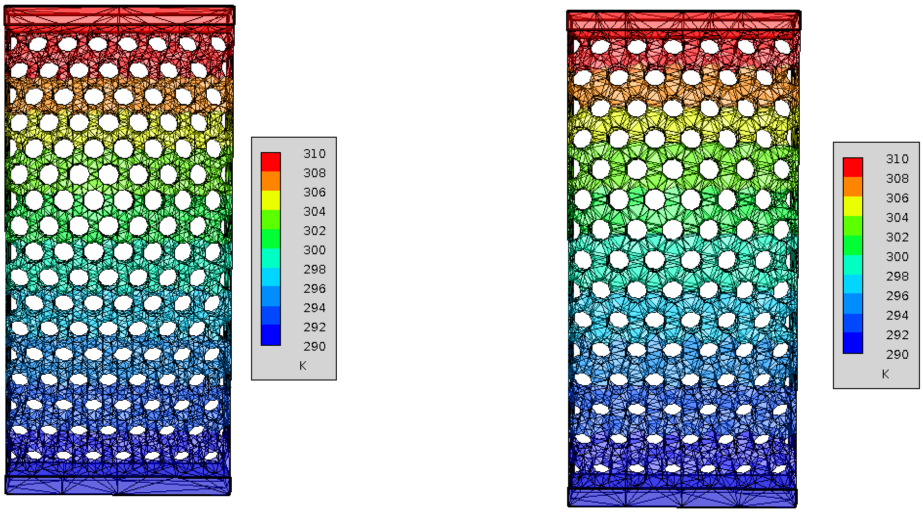

Figure 3.11: 500 × 100 × 1000 nm device with 50% porosity (left) and 35% porosity (right) using a hexagonal arrangement of the holes. The prescribed temperature distribution is indicated by the color gradient. Thin black lines represent the simulation grid.

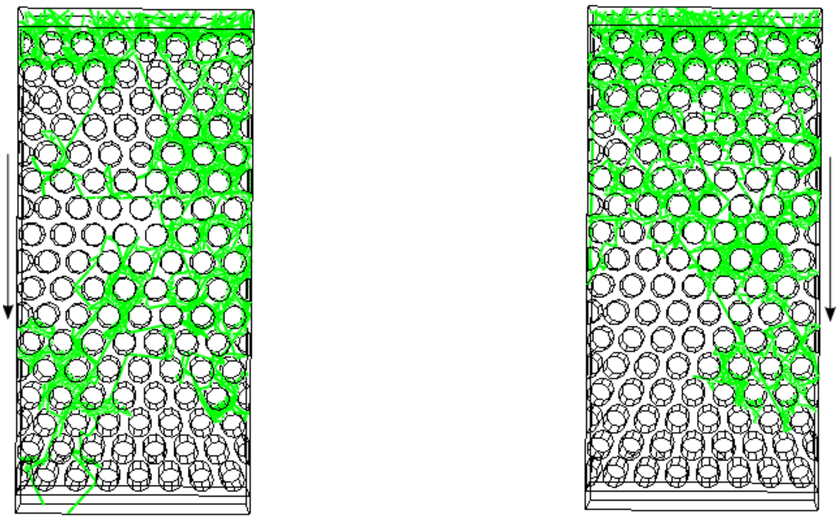

Figure 3.12: Phonon trajectories (green lines) in a 500 × 100 × 1000 nm device with 50% porosity using a hexagonal alignment of the holes for specularity parameter $p = 1.0$ (left) and $p = 0.1$ (right). The arrows indicate the direction of the flow.

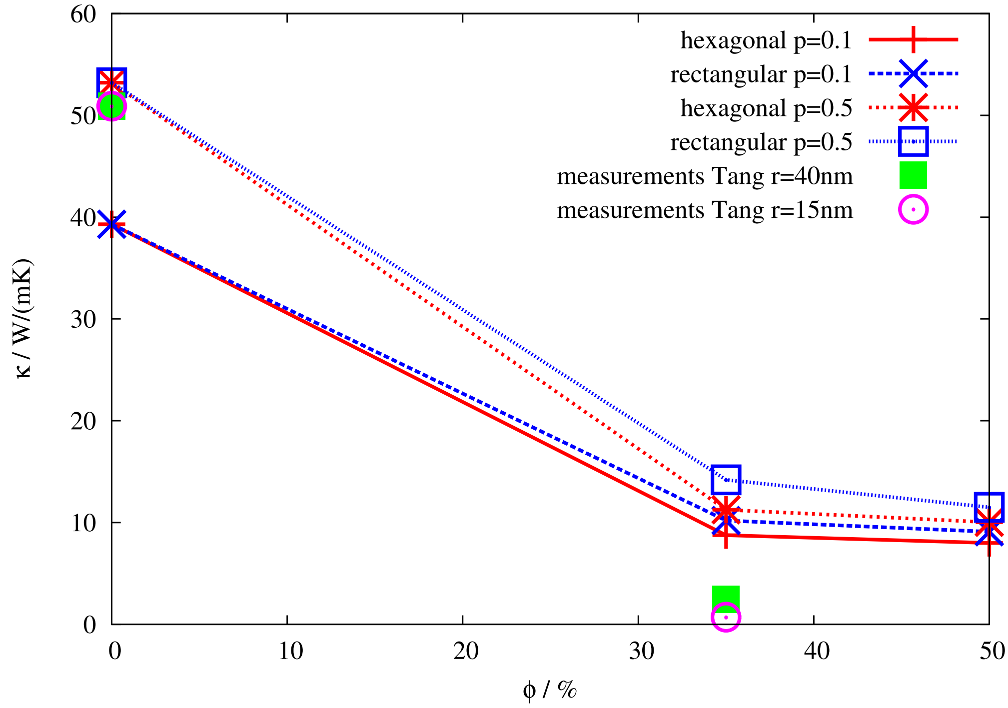

Figure 3.13: Thermal conductivity of the Si nanomesh over porosity ϕ comparing a hexagonal (red lines) and a rectangular (blue lines) arrangement of the holes. The specularity parameter is $p = \{0.1, 0.5, 1.0\}$. Measurement data from Ref. [14].

Chapter 4

Conclusion

In this work, a general procedure to solve the Boltzmann transport equation for phonons has been described and implemented. The Monte-Carlo method is used to solve the BTE for arbitrary complex 3D geometries.

Simulations have been carried out to calculate the time-of-flight (TOF) of phonons in dependence of geometric aspects of the device such as lengths or surface roughness considering boundary scattering limited transport. We found that diffusive surface scattering increases the TOF and plays an important role for small cross sectional areas and dimensions below 100 nm.

The procedure has been successfully validated against experimental data for bulk Si for a temperature range of 15 K to 400 K using phonon-phonon scattering and a mean free path-dependent scaling factor to account for size effects.

Finally, the simulator has been applied to nanomeshes in form of nanoporous Si membranes. The thermal conductivity at room temperature has been calculated for two arrangements of holes: rectangular and hexagonal. A decrease of the thermal conductivity has been observed with increasing porosity and diffusive scattering for both structures.

Bibliography

[1] C. Kittel, *Introduction to Solid States Physics*, John Wiley & Sons Inc., 1986, Eight Edition.

[2] E. Pop, R.W. Dutton, K.E. Goodson, *Analytic band Monte Carlo model for electron transport in Si including acoustic and optical phonon dispersion*, J. Appl. Phys 96, 4998 (2004).

[3] J.M. Ziman, *Electrons and Phonons: The Theory of Transport Phenomena in Solids*, Claredon Press, Oxford, 1960.

[4] S. Mazumder, A. Majumdar, *Monte Carlo Study of Phonon Transport in Solid Thin Films Including Dispersion and Polarization*, J. Heat Transfer 123, 749 (2001).

[5] D. Lacroix, K. Joulain, D. Lemonnier, *Monte Carlo transient phonon transport in silicon and germanium at nanoscales*, Phys. Rev. B 72, 064305 (2005).

[6] C. Jacoboni, L. Reggiani, *The Monte Carlo method for the solution of charge transport in semiconductors with applications to covalent materials*, Rev. Mod. Phys. 55, 645 (1983)

[7] M.G. Holland, *Analysis of Lattice Thermal Conductivity*, Phys. Rev. 132, 2461 (1963)

[8] Z. Stanojevic, *Simulation of Carrier Transport in Ultra-Thin-Body Devices*, Diploma thesis.

[9] A. Majumdar, C.L. Tien, and F.M. Gerner, *Microscale Energy Transport*, Taylor & Francis, 1998.

[10] J. Dubois, E. Belin-Ferré, K. Urban, *Complex Metallic Alloys: Fundamentals and Application*, Wiley, 2010, First edition.

[11] W. Demtröder, *Experimentalphysik 2*, Springer; 2008, Fifth edition.

[12] C. Jeong, S. Datta, M. Lundstrom, *Thermal conductivity of bulk and thin-film silicon: A Landauer approach*, J. Appl. Phys. 111, 093708 (2012)

[13] M-H. Bae, Z. Li, Z. Aksamija, P.N. Martin, F. Xiong, Z-Y. Ong, I. Knezevic and E. Pop, *Ballistic to diffusive crossover of heat flow in graphene ribbons*, Nature Comm., 4, 1734 (2013)

[14] J. Tang, H-T. Wang, D.H. Lee, M. Fardy, Z. Huo, T.P. Russell, P. Yang *Holey Silicon as an Efficient Thermoelectric Material*, Nano Lett., 10, 4279 (2010)

[15] A.I. Boukai, Y. Bunimovich, J. Tahir-Kheli, J.K. Yu, W.A. Goddard, J.R. Heath, *Silicon nanowires as efficient thermoelectric materials*, Nature 451(7175), 168-171 (2008)

[16] A.I. Hochbaum, R. Chen, R.D. Delgado, W. Liang, E.C. Garnett, M. Najarian, A. Majumdar, P. Yang, *Enhanced thermoelectric performance of rough silicon nanowires*, Nature 451, 163-167 (2008)

[17] *http://www.globaltcad.com*

[18] H. Karamitaheri, personal communication

[19] G. Nilsson and G. Nelin, *Study of the Homology between Silicon and Germanium by Thermal-Neutron Spectrometry*, Phys. Rev. B 6, 3777 (1972)